Aalto University
School of Engineering
Department of Mechanical Engineering

Unto Kujansuu

Implementation of a One-equation Local Correlation-Based Transition Model

Master's Thesis
Espoo, September 11, 2017

Supervisor: Prof. Jukka Tuhkuri
Advisor: Prof. Timo Siikonen

Aalto University
School of Engineering

ABSTRACT OF
MASTER'S THESIS

Author
Unto Kujansuu

Title
Implementation of a One-equation Local Correlation-Based Transition Model

Unit Department of Mechanical Engineering

Date September 11, 2017 **Number of pages** ix + 85

Minor Fluid Mechanics **Code** K3006

Supervisor Professor Jukka Tuhkuri
Advisor Professor Timo Siikonen

Transition is a common phenomenon in which a laminar flow becomes turbulent through a complicated process that drastically changes the flow characteristics. Since this phenomenon is present in practically all engineering applications, the ability to predict the transition plays a significant role in computational fluid dynamics (CFD). However, the current techniques for Reynolds-Averaged Navier-Stokes (RANS) simulations comprise of a rather complex formulation and are therefore difficult to implement and fine-tune for varying flow conditions.

In this thesis, a promising One-equation Local Correlation-based Transition Model is implemented into OpenFOAM CFD software, for which procedure a detailed tutorial is provided. The implementation is validated by running simulations with standard zero pressure gradient flat plate cases. Furthermore, the model response for varied inlet conditions is studied by examining the effect of eddy viscosity ratio and freestream turbulence intensity, and a new approach of coupling the transition model with the SST-sust turbulence model is proposed.

The simulation results show that the implemented transition model predicts correctly the transition in zero pressure gradient flat plate cases and the estimated skin friction coefficient is in good accordance with experimentally obtained results. Furthermore, the studies indicate that a consistent behaviour for the transition model is achieved when coupled with a turbulence model with sustained turbulence.

Keywords transition, LCTM, turbulence, OpenFOAM, CFD, RANS

Language English

Aalto-yliopisto
Insinööritieteiden
korkeakoulu

DIPLOMITYÖN
TIIVISTELMÄ

Tekijä
Unto Kujansuu

Työn nimi
Paikallisiin korrelaatioihin perustuvan yksi-yhtälö transitiomallin implementointi

Laitos Konetekniikan laitos

Päivämäärä 11. syyskuuta 2017 **Sivumäärä** ix + 85

Sivuaine Virtausmekaniikka **Koodi** K3006

Valvoja Professori Jukka Tuhkuri
Ohjaaja Professori Timo Siikonen

Transitio on luonnossa yleisesti esiintyvä ilmiö, jossa laminaari rajakerrosvirtaus muuttuu turbulentiksi monimutkaisen prosessin aikana samalla muuttaen merkittävästi virtauksen ominaisuuksia. Transition ennustamisella on merkitys laskennallisessa virtausmekaniikassa, sillä tämä ilmiö esiintyy lähes kaikissa luonnollisissa virtauksissa ja virtauskoneissa. Nykyiset ajan suhteen keskiarvoistetuihin Navier-Stokes yhtälöihin perustuvat transition huomioivat laskentamallit rakentuvat kuitenkin perin monimutkaisten yhtälöiden varaan, täten hankaloittaen mallien implementoimista ja hienosäätöä erilaisiin virtaustilanteisiin.

Tässä diplomityössä implementoidaan lupaava paikallisia korrelaatioita käyttävä yksi-yhtälö transitiomalli avoimeen lähdekoodiin perustuvaan OpenFOAM virtauslaskenta-ohjelmistoon. Lisäksi tähän toimenpiteeseen esitetään yksityiskohtainen tutoriaali, joka mahdollistaa mallin implementoinnin ohjelmistoon Linux-ympäristössä. Transitiomalli validoidaan standardeilla nolla-painegradientti tasolevy-tapauksilla. Tämän lisäksi transitiomallin toimintaa analysoidaan suorittamalla simulointeja erilaisilla pyörreviskositeetin suhteilla sekä vapaan virtauksen turbulenssin intesiteetin arvoilla tulovirtauksen reuna-ehdossa.

Simulaatioiden tulosten perusteella voidaan todeta ennustetun transition ja pintakitkakertoimen vastaavan hyvällä tarkkuudella aikaisemmin esitettyjä kokeellisia tuloksia sekä mallilla suoritettuja tutkimuksia. Lisäksi analyysin tulokset viittaavat mallin kykenevän johdonmukaisempaan transition mallintamiseen tämän ollessa kytkettynä turbulenssimalliin, joka säilyttää virtauksen turbulenssin vakiona.

Asiasanat transitio, LCTM, turbulenssi, OpenFOAM, CFD, RANS

Kieli Englanti

Acknowledgements

First of all, I would like to express my sincere appreciation to my thesis supervisor Professor Jukka Tuhkuri for his constant guidance throughout my studies. I would also like to thank my thesis advisor Professor Timo Siikonen for giving me this great opportunity to work on the topic of transition modelling and for providing his assistance through this challenging project. Without his insight and general guidance, none of this would have been possible. I must also extend my gratitude to the fellow staff at the department for creating such an open, inspiring environment to work in. It was a privilege to getting to know you all.

Finally, I would like to express profound gratitude to my parents and to my girlfriend Johanna for providing me with unfailing support and continuous encouragement throughout my years of study and through the process writing this thesis. This accomplishment would not have been possible without them. Thank you.

Espoo, September 11, 2017

Unto Kujansuu

Symbols and Abbreviations

Roman Symbols

a	acceleration
C_f	skin friction coefficient
d_w	wall distance
E	destruction term
E_t	total energy
e	specific internal energy
F	force
F_{length}	transition length constant
F_{onset}	transition trigger function
f	cell face
g	gravitational acceleration
h	enthalpy
k	turbulence kinetic energy, roughness element height, thermal conductivity
m	mass
P	source term
p	pressure
Q	amount of heat
Q_ϕ	source term
$\mathbf{r}$	distance vector
R	cell expansion ratio
Re	Reynolds number
Re_c	critical Reynolds number
$Re_{\theta t}$	transition onset momentum thickness Reynolds number
Re_V	local vorticity Reynolds number
S	strain rate magnitude
S_{ij}	strain rate tensor
$\mathbf{S}$	face-area vector
s	streamwise direction
T	temperature, large time scale
t	time
Tu	turbulence intensity

U	characteristic velocity, local velocity
U_∞	freestream velocity
u^+	dimensionless velocity
u_τ	friction velocity
$\overline{u}$	time-averaged velocity
u'	fluctuating velocity component
V	volume, wall-normal velocity
W	amount of work
y	normal-to-wall distance
y^+	dimensionless wall distance

Greek Symbols

α	diffusion coefficient, turbulence model coefficient
β,β^*	turbulence model coefficients
$\delta_{99\%}$	boundary layer thickness
δ_{ij}	Kroenecker's delta
δ^*	boundary layer displacement thickness
Δ	change
γ	intermittency
θ	momentum thickness
κ	inner law constant
λ	second viscosity coefficient
λ_θ	pressure gradient parameter
$\lambda_{\theta L}$	local pressure gradient parameter
λ_{tr}	Thwaites' parameter
μ	dynamic viscosity
μ_t	turbulent dynamic viscosity
ν	kinematic viscosity
ν_t	turbulent eddy viscosity
ϕ	scalar
Φ	dissipation function
Π	Cole's wake parameter
ρ	density
σ	stress
τ_w	wall shear stress
ω	specific turbulence dissipation rate
Ω	magnitude of the absolute vorticity rate

Abbreviations

CFD	Computational Fluid Dynamics
DNS	Direct Numerical Simulation
FDM	Finite Difference Method
FEM	Finite Element Method
FVM	Finite Volume Method
HO	Higher-Order scheme
LCTM	Local Correlation-based Transition Model
LES	Large Eddy Simulation
PDE	Partial Differential Equation
RANS	Reynolds-Averaged Navier-Stokes equations
RSM	Reynolds Stress Model
SST	Shear Stress Transport
TMP	Template Metaprogramming
TS	Tollmien-Schlichting wave
TVD	Total Variaton Diminishing
UD	Upwind Differencing

Contents

Chapter 1

Introduction

Laminar-turbulent transition has been the focus of considerable theoretical, experimental and numerical work throughout the years due to its significant effect on the performance of many important fluid dynamical applications, such as airplanes, wind turbines and propellers. In this phenomenon, the flow characteristics are changed through an extremely complicated process, in which a laminar flow with a streamlined velocity profile transforms into a turbulent flow characterized by chaotic changes in multiple flow variables, such as in velocity and pressure. As a consequence, the transition has a significant effect on the overall properties of a flow. Therefore, an accurate prediction of the transition would allow designs that improve the efficiency of many fluid-dynamic processes.

Although the transition process has been under active research since the first studies conducted by Reynolds in 1885, there yet exists no fundamental understanding of all the mechanisms related to laminar-turbulent transition. The nature of this phenomenon is so complex that it is unlikely to be analytically solved in the short-term or even long-term future. However, the continually increasing calculation power of computers has made it possible to study the transition process with Computational Fluid Dynamics (CFD), allowing more accurate methods for numerical modelling of the phenomenon. Hence, it seems evident that future understanding of transition mechanisms will be obtained through numerical approaches.

Recent years have witnessed a transition modelling trend to shift towards computations with Large Eddy Simulation (LES) and Direct Numerical Simulation (DNS), mainly due to the better utilisation of parallelised calculation. Although these numerical methods have been shown to achieve excellent accuracy, they still require an excessive amount of computational power rarely available in common simulations. At the present time, the methods are generally applicable only for rather simple flow cases and are therefore usually unable to solve practical engineering problems related to fluid dynamical designing. For this reason, approaches that are less resource-intensive, such as those based on the Reynolds-Averaged Navier-Stokes (RANS) method, still remain a useful and an attractive option, especially, for general-industrial CFD simulations, for which transition modelling has long been an elusive target.

Over the last decade, much research have been devoted to a numerical modelling of the transition resulting in rich variety of approaches for RANS based simulations [2–6]. Two approaches stand out prominently as they have achieved wide popularity within transition modelling: the Local Correlation-based Transition Model (LCTM) by Langtry and Menter in 2006 [2], which is based on two transport equations and is generally known as the $\gamma - Re_{\theta t}$-model; and the Three-Equation Eddy-Viscosity Model, $k - k_L - \omega$, by Walters and Cokljact [3]. Especially the improved Langtry-Menter model from 2009 [7] has proven to function well in general flow cases. This is also highlighted in a recent review by Dick et al. [8] that compares current transition models in turbo-machinery simulations. $\gamma - Re_{\theta t}$-models overall functionality has yielded further model extensions to account for the effects of surface roughness (Lange et al. [9]) and crossflow (Müller et al. [10] and Langtry et al. [11]). However, it suffers from a rather high level of complexity, a common disadvantage in many transition models, which hinders its implementation for other turbulence models as well as its fine-tuning for specific flow conditions. Moreover, the Langtry-Menter transition model lacks Galilean invariance, which is a very beneficial feature for general CFD simulations.

In 2015, Menter et al. [1] introduced a new LCTM that is based on one transport equation and can be considered an enhanced version of the aforementioned $\gamma - Re_{\theta t}$ transition model. Not only does the new version, also referred to as the γ-model, enjoy the advantages of the simplified formulation, but it is also able to achieve the Galilean invariance by relying only on variables formulated in a local fashion. Therefore, the model can be considered to have a great potential within future transition modelling. However, to the best of authors' knowledge, no previous testing on this model has been conducted for validating the results of the original publication. Moreover, no implementation of the γ-model has been published for the open source software OpenFOAM [12], which would allow more straightforward large-scale testing and further development of the model.

The primary aim of this thesis is first to implement the γ-model [1] for OpenFOAM CFD software and then to validate the implemented model. The implementation is realized by modifying the C++ based OpenFOAM source code, where the transition model is coupled with the Shear Stress Transport (SST) $k - \omega$ turbulence model [13]. Next, the implemented model is verified against several computational grids as well as varying discretizations for divergence terms in order to ensure simulation independence from these factors. Using the obtained setup, the model is validated for a zero pressure gradient flat plate using four standard test cases. The results are compared against experimental values and ones obtained with the prior $\gamma - Re_{\theta t}$ transition model. The secondary objective of this work is to evaluate the model behaviour against modified inlet values of turbulent variables and to investigate the behaviour of a γ-model coupled with the Menter SST $k - \omega$ that uses a controlled decay [14]. In addition, this work aims to provide a tutorial of the γ-model implementation for OpenFOAM in the Linux environment. This thesis is a continuation of the prior work within transition modelling by Kruljevic [15].

The structure of this work is as follows. Chapter 2 presents the governing equations of a viscous flow and describes the fundamental physics of the boundary layer.

The next chapter defines the mathematical models and numerical methods used in this work for turbulence modelling. Chapter 4 introduces briefly the current techniques used in transition modelling followed by a detailed description of the one-equation LCTM in Section 4.2. In addition, a step-by-step guide for an implementation of the transition model is provided. Chapter 5 defines the case setups as well as presents the results of the simulations. Finally, the results are summarized and conclusions are drawn.

Chapter 2

Fundamentals of a Viscous Flow

Transition is a complex viscous-fluid phenomenon confined to a thin boundary layer. Although no fundamental understanding of the transition process exists, the boundary layer theory in conjunction with the equations of a viscous flow can be used to account for the effects of transition into calculations. This chapter presents the governing formulae of viscous flow as well as introduces the physical background of the boundary layer flow, in which all the fluid dynamic calculations and models in this thesis are based on. First Section 2.1 introduces the paramount equations that describe the motion of viscous flow, whereas Section 2.2 explains the physics of boundary layer as well as introduces the boundary layer theory. The final Section 2.3 describes the transition process including its governing mechanisms.

2.1 Governing equations

The governing equations that describe the motion of viscous flow have been known for over one hundred years and are based on three fundamental principles:

- Conservation of mass
- Conservation of momentum
- Conservation of energy

These three laws are the basis of fluid dynamics and comprise of five Partial Differential Equations (PDE): one for the conservation of mass, three for the conservation of momentum and one for the conservation of energy. In this thesis, these five PDEs are altogether referred to as the Navier-Stokes equations, which is also a common practice in CFD literature. However, to be precise, the term is valid only for the conservation of momentum equations. This formulae applies to all viscous fluid flows, and furthermore they are the foundation for all fluid dynamical calculations.

The above mentioned equations are derived for Newtonian, continuum fluids, which is also applied to fluids in this work. For Newtonian fluids, such as water, air and oil, the relationship of viscosity is linear to a strain rate. This denotes that the viscosity is dependent only on the temperature and pressure, whereas the viscosity

of non-Newtonian fluids is additionally affected by applied stresses, thus causing nonlinear behaviour.

2.1.1 Continuity equation

The main principle in the conservation of mass law, also known as the equation of continuity, postulates that mass cannot disappear by itself. This equation obtains a simple form with conventional representation:

$$m = \rho V = constant \tag{2.1}$$

where m denotes the mass, ρ the density and V the volume of a fluid element. However, equation (2.1) is only valid for fixed particles. An appropriate form for fluid flows can be obtained by first applying a time derivation followed by a division with volume:

$$\frac{D\rho}{Dt} + \rho \frac{DV}{Dt}\frac{1}{V} = 0 \tag{2.2}$$

in which t signifies the time. The latter part containing volume terms is connected to the following strain rate relations:

$$\mathrm{div}\mathbf{U} = \epsilon_{xx} + \epsilon_{yy} + \epsilon_{zz} = \frac{DV}{Dt}\frac{1}{V} \tag{2.3}$$

where div denotes the divergence operator, and $\mathbf{U}$ the velocity vector comprising of three components (u,v,w) according to Cartesian coordinate system (x, y, z). This notation for vectors will be used throughout the paper. The quantities ϵ_{xx}, ϵ_{yy} and ϵ_{zz} represent the normal-strain rates according to x, y and z axis, respectively. Applying the above shown relations in Equation (2.2) results in the general form of the continuity equation for fluids:

$$\frac{D\rho}{Dt} + \rho\,\mathrm{div}\mathbf{U} = 0 \tag{2.4}$$

The equation reduces to a simpler form in case of incompressible flow as density remains constant:

$$\mathrm{div}\mathbf{U} = 0 \tag{2.5}$$

2.1.2 Navier-Stokes equations

The Navier-Stokes equations are derived from the conservation of momentum principle, also known as Newton's second law, that is one of the fundamental laws of physics. This law connects the applied force proportionally to acceleration of particle mass:

$$\mathbf{F} = m\mathbf{a} \tag{2.6}$$

where $\mathbf{F}$ signifies the force vector, m the mass and $\mathbf{a}$ the acceleration of particle. A more suitable presentation for a fluid particle is achieved by diving the equation (2.6) with volume and rearranging the terms:

$$\rho\frac{D\mathbf{U}}{Dt} = \mathbf{f}_{\mathrm{body}} + \mathbf{f}_{\mathrm{surface}} \tag{2.7}$$

where $\mathbf{f}$ represents the applied force per unit volume on the fluid particle. Considering viscosity combined with the deformation law for a Newtonian fluid, the equation (2.7) leads to the Navier-Stokes equations that comprise of three equations according to the dimensions of Cartesian coordinate system (x, y, z). When expressed with indicial notation, a compact form for the equation is achieved:

$$\rho\frac{D\mathbf{U}}{Dt} = \rho\mathbf{g} - \nabla p + \frac{\partial}{\partial x_j}\left[\mu\left(\frac{\partial u_i}{\partial x_j} + \frac{\partial u_j}{\partial x_i}\right) + \delta_{ij}\lambda\,\mathrm{div}\mathbf{U}\right] \tag{2.8}$$

where $\mathbf{g}$ denotes the gravity vector, p the pressure and μ the viscosity. δ_{ij} and λ designate the Kroenecker delta operator and the second coefficient of viscosity, respectively. Although this fundamental equation is rigorous in describing viscous flow, it can be solved analytically only in simple flow cases due to its non-linear, complex characteristics. In case of an incompressible flow, equation (2.8) reduces to a somewhat simpler form.

$$\rho\frac{D\mathbf{U}}{Dt} = \rho\mathbf{g} - \nabla p + \frac{\partial}{\partial x_j}\left[\mu\left(\frac{\partial u_i}{\partial x_j} + \frac{\partial u_j}{\partial x_i}\right)\right] \tag{2.9}$$

The complete three-equation-form as well as the full derivation of the Navier-Stokes equations can be found, for instance, from White's textbook for viscous flows [16].

2.1.3 Energy equation

The energy equation is based on the first law of thermodynamics, which states that the total energy of an isolated system remains constant. In other words, energy can be neither created nor destroyed, it can merely transform to another form.

$$dE_t = dQ + dW \tag{2.10}$$

where E_t represents the total energy of the system, Q the amount of heat added and W the work done by system. For a fluid element, the total energy can be presented as the sum of internal, kinetic and potential energy per unit volume:

$$E_t = \rho\left(e + \frac{1}{2}\mathbf{U}^2 - \mathbf{g}\cdot\mathbf{r}\right) \tag{2.11}$$

in which the quantity e signifies the specific internal energy and $\mathbf{r}$ the distance vector. The general form of the energy equation can be derived from equation (2.10) by taking multiple principles of physics into account:

$$\rho\frac{Dh}{Dt} = \frac{Dp}{Dt} + \mathrm{div}(k\nabla T) + \Phi \tag{2.12}$$

where h denotes the enthalpy, p the pressure and t the time. The terms of the divergence operator, k and T, designate the thermal conductivity and the temperature, respectively. The last term, Φ, is commonly known as the dissipation function, which includes the viscous stress terms separated from the pressure. See for instance reference [16] for a energy equation derivation.

2.2 Boundary layer principles

The physics of the boundary layer have been the focus of considerable theoretical, numerical, and experimental research since the introduction of the boundary layer theory by Prandtl at the beginning of the 20th century. Although no fundamental understanding of transition nor turbulence yet exists, the extensive efforts within this subject have resulted in numerous useful tools that can be used for estimating the properties of the flow, such as skin friction, a flow separation and a pressure distribution. Thus, although not surprisingly, the concept of boundary layers has a great significance within the fluid mechanics.

A boundary layer is defined as the region of flow retardation that develops in the vicinity of bounding surfaces due to the fluid viscosity. The boundary layer features two types of flow regimes that significantly differ in characteristics: laminar and turbulent regimes. Figure 2.1 shows the connection between these two dissimilar flow regimes through a region known as transition, by illustrating a boundary layer development over a flat plate.

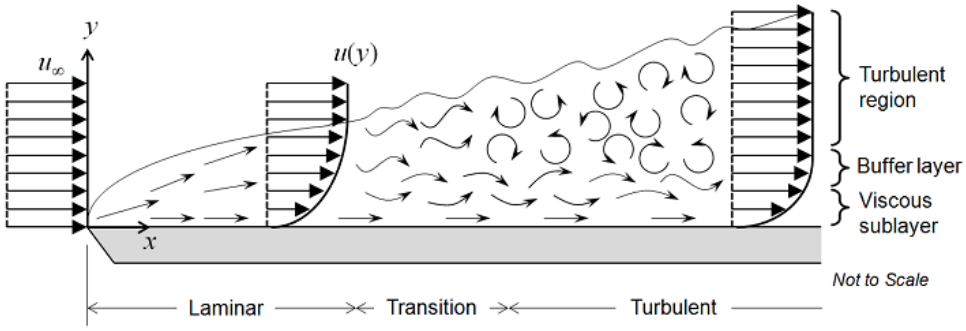

Figure 2.1: Boundary layer on a flat plate [17].

Consider the flow circumstance shown in Figure 2.1. Initially, a boundary layer flow starts to develop as laminar when uniform velocity fluid reaches the upstream bounding surface. The laminar flow is characterised by parallel velocity lines and a smooth velocity profile near the surface. Over some distance, minute disturbances called Tollmien-Schlicting waves begin to occur in the flow field, which can be considered as the start of the transition region. Oscillations and chaotic movements increase until eventually the entire flow field breaks down into a fully turbulent flow characterised by random changes in flow variables.

A transition between these two flow regimes is affected by multiple different factors, which are introduced at length in section 2.3. However, a specific dimensionless term can be considered as the primary controlling parameter for viscous flow. This term is known as the Reynolds number and can be used to predict the transition as well as the type of a flow in general. The Reynolds number represents the ratio

between inertial forces and viscous forces within a fluid that is given by

$$Re = \frac{\rho U_\infty L}{\mu} = \frac{U_\infty L}{\nu} = \frac{\text{inertial forces}}{\text{viscous forces}} \tag{2.13}$$

where U_∞ is the freestream velocity, L the characteristic length of the surface or the body, and μ the dynamic viscosity. The second form is to present the Reynolds number in terms of kinetic viscosity, ν, which eliminates the density, ρ, from the formulation. For a low Reynolds number, the boundary flow tends to be laminar whereas high values indicate a turbulent flow. However, the very beginning of the boundary layer is always laminar, and the transition point to turbulent flow depends on the Reynolds number in conjunction with other influencing factors.

As mentioned above, the laminar and the turbulent flow regimes deviate significantly from each other, and thereby the point of transition impacts the overall characteristics of the flow. The thinner laminar layer induces less skin friction, and thus reduces the overall drag of the surface in contrast to turbulent layer. This is due to the smaller amount of kinetic energy conveyed within the layer, which can also be seen as a smoother velocity profile in Figure 2.2. Consequently, the lack of momentum causes instabilities leading to a prior separation of the flow. In comparison, a turbulent flow is compromised by fluctuations, eddies and random variations in variables. Turbulent flow contains more momentum and thereby retains a higher velocity close to the wall, where it decelerates rapidly in very thin region, as can be observed in Figure 2.2. This allows the flow attaching to the surface longer preventing a flow separation. Although this increases the skin friction, it also enhances the mixing between layers making the phenomenon useful in certain fluid dynamical processes, such as in heat transfer applications. However, it is generally desirable to maintain boundary layer as laminar due to lower drag.

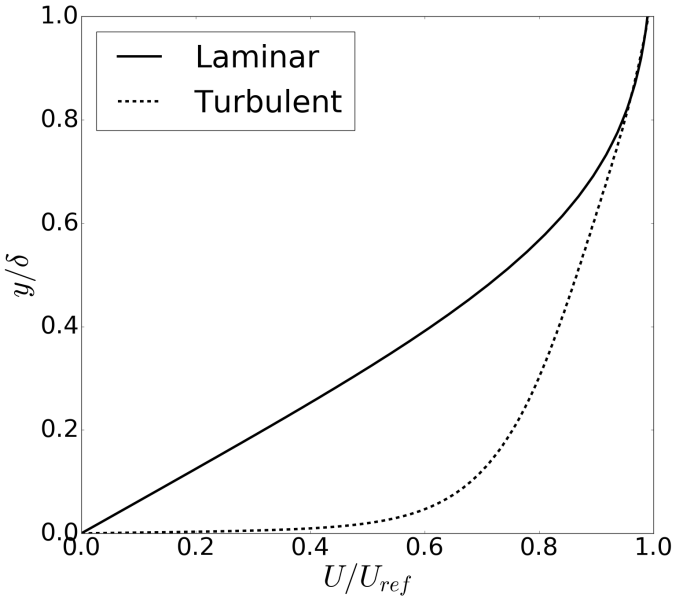

Figure 2.2: Laminar and turbulent velocity profiles.

The boundary layer analysis provides efficient techniques for solving the properties of boundary layers by simplifying the complex Navier-Stokes equations (2.8). Although not applicable to low Reynolds numbers (creeping flows) or flow separation, it offers exact solutions for laminar layers and accurate estimations for turbulent layers. The essential solutions for this work are shown as they are used for analyzing the simulation results.

Laminar boundary layer

For a two-dimensional flow, shear stresses in a boundary layer are given by

$$\tau = \mu \left(\frac{\partial u}{\partial y} + \frac{\partial v}{\partial x} \right) \tag{2.14}$$

The second term $\frac{\partial v}{\partial x}$ can often be considered negligible, thus the wall shear stresses can be approximated as follows:

$$\tau_w \approx \mu \left(\frac{\partial u}{\partial y} \right)_{y=0} \tag{2.15}$$

For a laminar layer, the Blasius solution provides means to calculate the boundary layer thickness, $\delta_{99\%}$, and the skin friction, C_f, for a flat plate flow [16]:

$$\frac{\delta_{99\%}}{x} \approx \frac{5.0}{\sqrt{Re_x}} \tag{2.16}$$

$$C_f = \frac{0.664}{\sqrt{Re_x}} \tag{2.17}$$

where x represents the distance on a flat plate and Re_x the Reynolds number in respect to the distance. Here, the boundary layer thickness, $\delta_{99\%}$, is defined as the distance normal-to-surface, where the boundary layer velocity reaches ninety-nine percent of the freestream velocity [16].

Turbulent boundary layer

For turbulent shear layers, no analytical solutions exists due to extremely complex structure of the phenomenon. However, much detail has been gained from experimental velocity profiles through a dimensional analysis, which introduces the following dimensionless quantities for velocity and distance:

$$u^+ = \frac{\overline{u}}{v^*}, \qquad y^+ = \frac{y v^*}{\nu} \tag{2.18}$$

where $\overline{u}$ designates the time-averaged velocity, y the distance from the wall and ν the kinematic viscosity of fluid. The variable v^* is known as wall-friction velocity and given by

$$v^* = \left(\frac{\tau_w}{\rho} \right)^{1/2} \tag{2.19}$$

where τ_w represents the wall shear stress and ρ the density. The characteristics of turbulent layer distinguish when written in terms of dimensionless parameters on a logarithmic scale, and are essential to understand for analyzing simulation results. The dimensionless profile is illustrated in Figure 2.3, which shows analytical fittings for a simulated turbulent boundary layer.

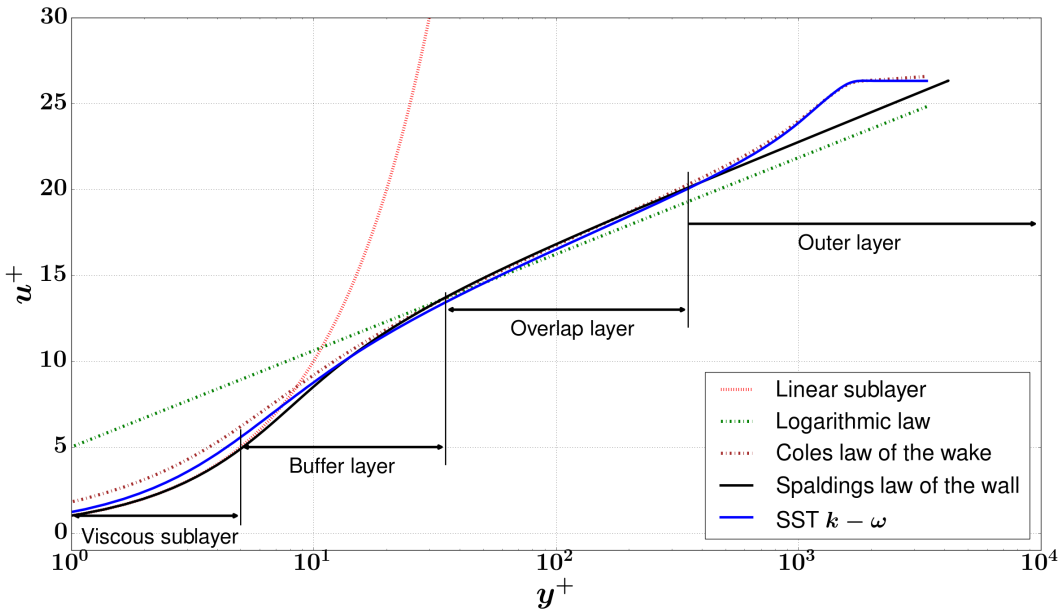

Figure 2.3: Turbulent boundary layer.

Turbulent boundary layers comprise of three regions that have different physical qualities [16]:

- **Viscous sublayer**: dominated by viscous (molecular) shear
- **Overlap layer**: both types of shears important
- **Outer layer**: dominated by turbulent (eddy) shear

The viscous sublayer, also known as the inner layer, is a very thin region ($y^+ \leq 5$) closest to the surface. The layer covers approximately 0.2% of the total boundary layer thickness. In the viscous sublayer, the turbulence is damped out by molecular viscosity resulting in a linear velocity profile that follows the curve $u^+ = y^+$.

The overlap layer is located approximately between $35 \leq y^+ \leq 350$ and covers the range 2 percent $\leq y/\delta \leq$ 20 percent of the total boundary layer thickness. Within the layer, the velocity profile follows logarithmic relation that is commonly referred to as the overlap log-law and is shown in Figure 2.3:

$$\frac{\overline{u}}{v^*} = \frac{1}{\kappa} \ln(\frac{yv^*}{\nu}) + B \tag{2.20}$$

where κ and B are universal constants that have values of 0.41 and 5.0 for a turbulent flow past smooth flat plate, respectively. The thin area located between $5 \leq y^+ \leq 35$

is referred to as the buffer layer. It connects and merges the viscous sublayer and the overlap layer, thus being neither logarithmic nor linear.

In 1961, Spalding [18] proposed a single formula for the "law of the wall" that is formulated as follows:

$$y^+ = u^+ + e^{-\kappa B}\left[e^{\kappa u^+} - 1 - \kappa u^+ - \frac{(\kappa u^+)^2}{2} - \frac{(\kappa u^+)^3}{6}\right] \tag{2.21}$$

in which the κ represents a constant for turbulent flow past smooth wall ($\kappa \approx 0.41$). Figure 2.3 illustrates how Spaldings law of the wall shows excellent fitting for the entire wall-related region excluding the region of wake in the outer layer when compared to the simulated dimensionless velocity profile with SST $k-\omega$ turbulence model.

A more accurate approximation for overlap and outer layers can be achieved with a log-law proposed by Cole [19] that contains a function for including the "wake" effects:

$$u^+ \approx \frac{1}{\kappa}\ln(y^+) + B + \frac{2\Pi}{\kappa} f\left(\frac{y}{\delta}\right) \tag{2.22}$$

where Π is the Coles' wake parameter and $f(\frac{y}{\delta})$ the wake function. As shown in Figure 2.3, Coles' law of the wake agrees well with simulated results within overlap and outer regions whereas loses its accuracy closer to the surface.

For calculating the skin friction, C_f, on a flat plate, White recommends the following formula for turbulent flow [16]:

$$C_f \approx \frac{0.455}{\ln^2(0.06Re_x)} \tag{2.23}$$

The boundary layer thickness, $\delta_{99\%}$, can be calculated applying the following equation based on power-law expressions:

$$\frac{\delta_{99\%}}{x} \approx \frac{0.16}{Re_x^{1/7}} \tag{2.24}$$

2.3 Physics of the boundary layer transition

Extensive number of analytical and experimental studies have shown that a transition process can be divided into different stages according to the gradual growth of flow instabilities. The lack of stability results from environmental disturbances in the flow field caused by a number factors, including initial values and local variables of the flow. Consequently, a breakdown can occur via multiple different paths through the stages depending on numerous variables and the way these interact with each other, for determination of which no mathematical model exists.

Besides the aforementioned critical Reynolds number that can be defined for each flow through experimental studies to estimate its type, a theoretical approach known as the linearized stability theory can be used to predict the primary instability modes within the boundary layer flow. The idea is to solve a set of linear equations for

disturbances obtained from the nonlinear Navier-Stokes equations (2.8) by assuming small disturbances. The best known example of this is the Orr-Sommerfeld equation that estimates the occurrence of Tollmien-Schlichting (TS) waves which are the first signs of instability within a laminar boundary layer [20]. Some transition prediction methods, such as e^N, use this approach for determining the critical Reynolds number, which designates the onset of transition.

To exemplify the different features of the transition process, Figure 2.4 visualizes a natural transition process, which includes sequential behaviour and gradually propagating instabilities.

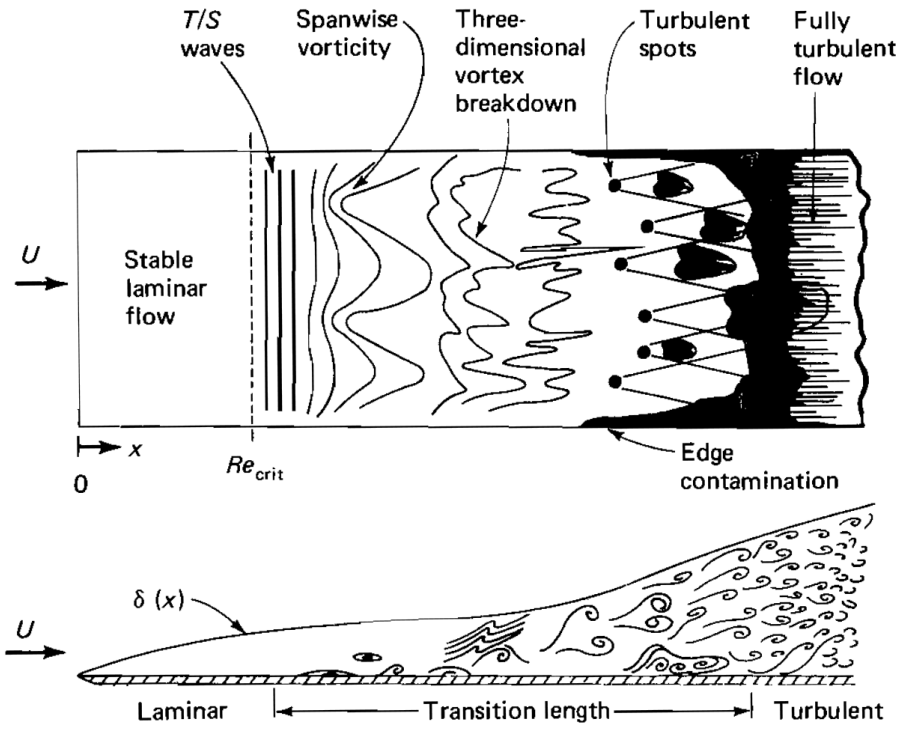

Figure 2.4: Natural transition on a flat plate [16].

Consider the natural transition shown in Figure 2.4, in which the disturbances can be seen to propagate through different phases. Initially, a stable laminar boundary layer starts to develop near the leading edge. After the critical Reynolds number, two-dimensional Tollmien-Schlichting waves begin to emerge in the flow. These linear, infinitesimal disturbances grow steadily into spanwise vorticities, which further develop to three-dimensional vortexes. The vortexes suffer a nonlinear break down at regions of a high localized shear causing fluctuations in velocity and pressure. This is followed by the emerge of local turbulent spots in the boundary layer. Finally, these spots coalesce and turn the boundary layer into a fully turbulent flow. [16]

2.3.1 Transition mechanics

A natural transition (Figure 2.4) is rather an exception than a rule in practical engineering applications, since disturbances in the flow can cause transition to proceed through alternative paths. Figure 2.5 describes these optional paths for external flows. This concept was first introduced in 1994 by Morkovin [21], however, it should be noted that other categorizations for the transition process exists in the literature as well, since interacting mechanisms still remain without complete understanding.

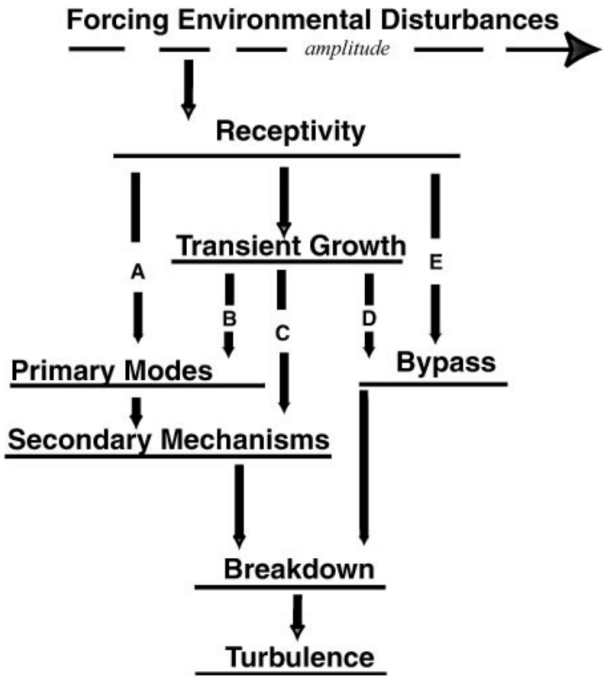

Figure 2.5: Different paths to transition [21].

Figure 2.5 demonstrates that a path of transition depends on the amplitudes of freestream disturbances entering the boundary layer. In case of small disturbances, the instabilities grow first through linear primary modes that can be estimated with linearized stability theory. When primary modes achieve a sufficient magnitude, they trigger the nonlinear, secondary instability mechanisms that eventually lead to a turbulent breakdown of the flow. However, as the environmental disturbances attain sufficiently high amplitudes, the primary mode development is surpassed and the transition proceeds directly through nonlinear paths. [21]

The level of distortion initiated in the boundary layer further relies on a flow receptivity to outside interferences, which can be considered as an independent process. This concept was introduced in 1969 by Morkovin [22], but its theory lies beyond the scope of this thesis. For more information, the reader should view for instance the reference [23], which offers an excellent review on the subject.

A transition process can be considered to proceed via three principal paths [16]:

1. **Natural Transition**. Occurs if the levels of environmental disturbances remain weak, also illustrated in Figure 2.4. The transition proceeds through path A, Figure 2.5, in which the initial growth of disturbances can be described with the linear stability theory (primary modes).

2. **Bypass Transition**. The stable laminar layer suddenly witnesses a three-dimensional vortex breakdown, thus surpassing the initial stages in natural transition. Corresponds to path E in Figure 2.5 and caused by large environmental disturbances, such as high freestream turbulence intensity ($Tu > 1\%$) or surface roughness.

3. **Intermediate Mechanisms**. Studies have shown transition to proceed through nonlinear, secondary mechanism defined as the transient growth, which can result in a number of paths (B,C and D in Figure 2.5) depending on the flow receptivity [23]. A transition induced by a specific phenomenon, such as a separation bubble or a wake, can be considered to represent the intermediate mechanisms.

In addition, a turbulent flow may reverse back to laminar under conditions of strong acceleration. This phenomenon is generally known as the relaminarisation, for which additional information can be found e.g. from reference [24].

2.3.2 Factors affecting transition

Over the years, much research has been directed toward experimental studies in order to determine all the affecting factors, as well as their involving mechanism in transition process. As a consequence, a number of somewhat precise correlations have been determined for several arguments, including freestream turbulence intensity, pressure gradient and surface roughness. These correlations function as the basis for the current methods predicting transition onset. This section provides a brief description of affecting parameters focusing especially on those relevant to the current transition models.

Pressure gradient

The freestream pressure gradient has a varying effect on the transition onset depending on its sign: Adverse pressure gradient destabilizes the laminar boundary layer and causes the transition point to shift upstream whereas a favorable pressure gradient stabilizes the flow and delays the transition. The streamwise pressure gradient at the edge of boundary layer is commonly described with Thwaites' parameter:

$$\lambda_{tr} = \frac{\theta^2}{\nu}\frac{dU}{ds} \tag{2.25}$$

where ν is defined as the kinematic viscosity, U the mean freestream velocity and s the streamwise direction. The variable θ signifies the momentum thickness given

by the following integral relation for two-dimensional boundary layer [16]:

$$\theta = \int_0^\infty \frac{\overline{u}}{U}\left(1 - \frac{\overline{u}}{U}\right) dy \tag{2.26}$$

where $\overline{u}$ is the mean velocity component. Over the years, various correlations have been suggested to model the effect of pressure gradient within the transition prediction. These correlations are based on varying theoretical approaches fitted into experimental data and are generally out of the scope of this thesis. However, a simple yet effective approach, known as one-step method of Michel, can be presented as an example. This method originating from the year 1952 predicts transition using only local values of momentum thickness and position:

$$Re_{\theta,tr} \approx \frac{U(x)\theta(x)}{\nu} \approx 2.9 Re_{x,tr}^{0.4} \tag{2.27}$$

where $U(x)$ and $\theta(x)$ indicate to local values of the velocity and the boundary layer thickness, respectively.

Freestream turbulence intensity

The freestream turbulence intensity, Tu, is a parameter used for describing the level of turbulence in freestream and is formulated as follows:

$$Tu = \frac{\sqrt{\frac{1}{3}(u'^2 + v'^2 + w'^2)}}{U} \tag{2.28}$$

where $u', v'$and w' are the fluctuating velocities and U the mean freestream velocity from Reynolds averaging. Several studies have demonstrated this parameter to have a significant effect on the transition. Flat plate experiments by Schubauer and Skramstad in 1947 showed that increment of turbulence intensity (to $Tu = 0.35\%$) from undisturbed values ($Tu = 0.02\%$) resulted in 50% reduction of the Reynolds number for transition, Re_{tr}, i.e., the transition took place half the distance than in the undisturbed flow [25]. In 1972, Dunham [26] developed a correlation for the momentum thickness Reynolds number, $Re_{\theta,tr}$, that combined the effects of turbulence intensity and pressure gradient:

$$Re_{\theta,tr} \approx (0.27 + 0.73e^{-80Tu})\left[550 + \frac{680}{(1 + 100Tu - 21\lambda_{tr})}\right] \tag{2.29}$$

where λ_{tr} signifies the Thwaites parameter defined by equation (2.25). This correlation is illustrated in Figure 2.6, which portrays the transition onset with different freestream turbulence values.

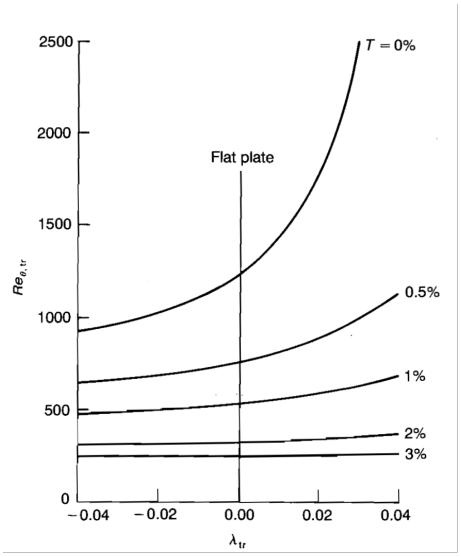

Figure 2.6: The combined effects of freestream turbulence and pressure gradient on transition [16].

The influence of the pressure gradient clearly decreases as the freestream noise increases. Generally, these large turbulence intensities ($Tu > 1\%$) also cause flow to skip the natural transition, which results in a *bypass* transition mechanism.

Several other correlations for the turbulence intensity have been developed that are widely used; for instance, a correlation by Van Driest and Blumer [27] for Falkner-Skan wedge flows, and a correlation suggested by Abu-Gannam and Shaw [28]. The latter correlation is formulated as follows:

$$Re_{\theta,tr} = 163 + e^{6.91-Tu} \tag{2.30}$$

This formulation is also utilized by Menter [1] transition model presented in Chapter 4.

Surface roughness

So far, all the presented correlations have presumed a smooth surface on the bounding walls. This assumption, however, is often invalid since surface roughness has been observed to significantly alter the flow characteristics. The roughness of the surface induces additional fluctuations in the flow that increase the turbulent kinetic energy production, which leads to thickening of the boundary layer [9]. Consequently, the transition is accelerated and shifted towards the leading edge.

A wall roughness can be considered to be either two-dimensional or three-dimensional depending on its geometry. Additionally, the three-dimensional roughness can be classified into two subsets: an isolated element and a distributed roughness. A wire or a cylinder across the flow defines a two-dimensional roughness, whereas three dimensional roughness element includes geometries like a spike or grain of sand in the surface. Studies have shown these three types of roughness yielding dissimilar effects in the flow field depending on three characterizing factors: height, shape, and

distribution. The correlation between these quantities has proven to be remarkably complex, however, some specific features have been identified. [16]

Disturbances induced by a two-dimensional wire depend on the ratio between wire height and the boundary layer displacement thickness k/δ^*. While this ratio stays below value 0.3, the flow remains unaffected. However, exceeding this ratio induces disturbances into the laminar flow, thus shifting the transition towards the roughness element according to the following correlation that is called as the local roughness Reynolds number:

$$Re_k = \frac{Uk}{\nu} \approx 850 \tag{2.31}$$

where k denotes the trip wire height. This determines a characteristic limit for a flat plate, below which the surface can be considered smooth. However, the effects of the two-dimensional roughness diminish when the Mach number increases, as shown in table 2.1.

Table 2.1: Effect of a Mach number on the flat plate (2D) [29].

Mach number	$\frac{Uk}{\nu}$
0.0	850
2.0	2000
4.0	10000

In comparison with the two-dimensional element, a single three-dimensional roughness element requires approximately double the height to induce turbulence into the flow ($k/\delta^* > 0.6$). When this point is exceeded, $Re_{\delta^*_{tr}}$ drops rapidly and a wedge of continuous turbulence is formed downstream of the roughness element. Thereby, a three-dimensional element is locally more critical, however, it endures significantly higher Mach numbers than the effect caused by two dimensional roughness and remains effective until $Ma > 0.4$. [16]

Distributed three-dimensional roughness is far less studied in contrast to single three-dimensional elements due to the difficulty for capturing details using experimental techniques. However, experimental studies have shown distributed roughness to have differing influence mechanism as single elements. For distributed sand-grain roughness, the local roughness Reynolds number has observed to have value of 120 ($Re_k \approx 120$) above which the transition moves rapidly towards the roughness.

Leading edge sweep

A flow over swept wings is governed by a phenomenon known as a crossflow. It has been observed to destabilize the secondary instabilities in the boundary layer flow [30]. As a result, the transition can onset locally well before the generation of the TS waves, thus cannot be predicted by the linear theory. This phenomenon is an inherent property of three-dimensional boundary-layer flows and closely connected to the flow receptivity for traveling as well as stationary waves [31].

Crossflow instabilities arise due to the imbalance of pressure and centrifugal forces inside the boundary layer. The centrifugal forces, caused by the in-plane curvature of the streamlines, are balanced by the pressure outside the boundary layer. However, inside the boundary layer the pressure remains somewhat constant whereas the centrifugal forces decrease closer to the surface as they correspond to local velocities. As a consequence, the supplementary pressure forces generate a crossflow within the boundary layer [30]. This effect is shown in Figure 2.7 which illustrates a three-dimensional boundary layer velocity profile affected by crossflow.

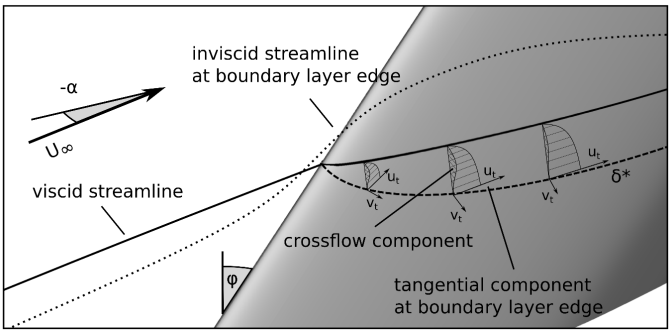

Figure 2.7: Boundary layer velocity profile curved by the crossflow components [10].

As shown in Figure 2.7, the induced crossflow changes the streamline curvature of a flow, resulting in a transverse velocity profile with an inflection point. This causes inflectional instabilities in the regions of high crossflow velocity gradients. Hence, the influence of a crossflow phenomenon is strongest, for instance, near the leading edge of a swept swing. [10, 32]

Chapter 3

Modelling of a Turbulent Fluid Flow

Chapter 2 presented the governing equations as well as the fundamental physics behind the boundary layer flows. In order to obtain a numerical solution for these type of flows, a large set of varying methodologies is provided by CFD that can be applied in simulations. First, this very complex phenomenon requires an approximation with a mathematical model, for which CFD features different techniques. Furthermore, for each mathematical approach various different numerical methodologies can be utilized depending on flow characteristics and the applied method itself. In order to elucidate a typical simulation process, it can be divided into several steps on the grounds of different methodologies involved in computation [33]:

- **Level of Approximation**: Definition of the mathematical model
- **Discretization**: Discretization of the computational domain and governing equations
- **Numerical Schemes**: Numerical methodology used for solving PDE's
- **The solution algorithms**: Computational algorithms to solve algebraic system of equations
- **Post-processing**: Techniques for manipulation and visualization of the computed flow field

This chapter follows the structure above in describing the methodology applied in this work. The first section 3.1 presents the principles of the Reynolds-Averaged Navier-Stokes (RANS) approximation and defines the SST $k-\omega$ turbulence model. The following sections 3.2 and 3.3 describe the discretisation phase with Finite Volume Method (FVM) and the numerical schemes involved. The solution algorithm and post-processing methods are presented in sections 3.4 and 3.5, respectively.

It is important to emphasize that choosing a suitable approach always requires first a definition of the flow characteristics, as well as the required level of approximation. This thesis examined external viscous flow cases with steady turbulence *i.e.*, the flow is statistically time independent. In addition, incompressibility and Newtonian fluid were assumed in all the case studies. Determining the level of

approximation virtually stands for choosing a mathematical method for modelling the governing equations. In this work, all the cases were simulated with turbulence models based on Reynolds-Averaged Navier Stokes (RANS) approach, which was an obvious choice due to the fact that One-equation Local Correlation-Based transition model was developed for RANS-based turbulence models.

3.1 Level of approximation: Reynolds-averaged Navier-Stokes

This work uses the Reynolds-Averaged Navier-Stokes (RANS) simulation which is a statistical approach for approximating a turbulent flow. Principles of the RANS method were introduced over a century ago by Reynolds, however, the equations are still extensively used within modern-day numerical simulations. The approach is based on a technique where the Navier-Stokes equations (2.8) are approximated by averaging them with respect to the time. The RANS simulation differs from two other widely utilized approaches, a Large Eddy Simulation (LES) and a Direct Numerical Simulation (DNS), in the level of modelling the turbulence. RANS methods model the entire turbulence whereas the DNS technique computes all the turbulent fluctuations in space and time. The Large Eddy Simulation settles itself between the two above mentioned concepts as it computes the most of turbulence spectrum and models only the smallest turbulence scales.

3.1.1 Reynolds averaging

Consider a turbulent flow characterized by random three dimensional changes and fluctuations in pressure, velocity and temperature. Assuming a steady turbulent flow, *i.e.*, the average values of the turbulent quantities do not vary with the time. Thus, a mean value for any turbulent quantity can be defined as follows:

$$\overline{Q} = \frac{1}{T}\int_{t_0}^{t_0+T} Q(t)dt \tag{3.1}$$

where T denotes the time scale that is large in comparison to the fluctuations time period. It should be noted that the time averaging is generally applied on certain transient turbulent flows as well, although the method is not formally valid for such cases. In these instances, the mean quantities are assumed to vary slowly with respect to time, thus the time scale, T, has to be small compared to the large-scale unsteadiness. When applied on velocity, the following definition for the mean value is achieved:

$$\overline{u} = \frac{1}{T}\int_{t_0}^{t_0+T} u(x,t)dt \tag{3.2}$$

According to the approach by Reynolds, variating quantities can be presented as the sum of a mean and a fluctuating part. For instance, the velocity components

can be presented as follows:

$$u = \overline{u} + u' \tag{3.3}$$
$$v = \overline{v} + v' \tag{3.4}$$
$$w = \overline{w} + w' \tag{3.5}$$

where $\overline{u}$ is the time averaged velocity and u' denotes the fluctuating part of the velocity. Figure 3.1 illustrates this approach as well as elucidates the difference between a steady and an unsteady turbulent flow.

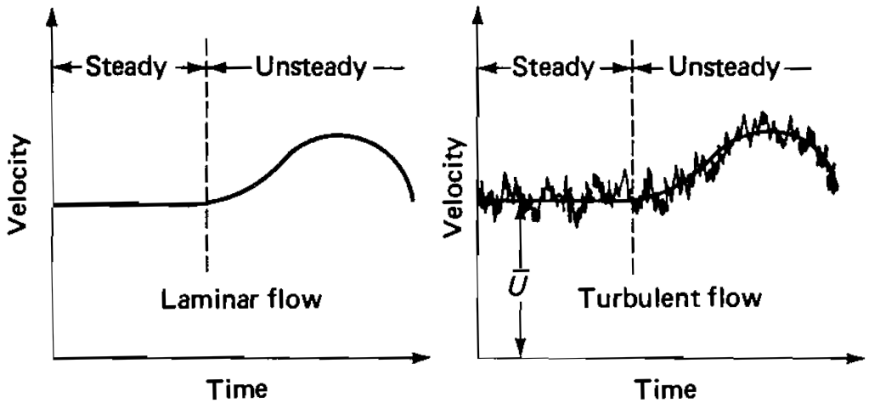

Figure 3.1: Steady and unsteady flows [16].

Applying the Reynolds averaging procedure to the incompressible continuity equation (2.5) results in an outcome similar to the original equation:

$$\frac{\partial \overline{u}}{\partial x} + \frac{\partial \overline{v}}{\partial y} + \frac{\partial \overline{w}}{\partial z} = 0 \tag{3.6}$$

Since the fluctuating terms u', v' and w' are linear, they have a mean value of zero, which results them in vanishing from the mean continuity equation. However, when the same procedure is applied on the nonlinear Navier-Stokes equations (2.8), all the fluctuating terms do not vanish because the mean value of a product comprising two fluctuating quantities *e.g.* $\overline{u'v'}$ cannot be presumed to equal zero. Using the indicial notation, the resulting equation can be expressed as follows:

$$\rho \frac{D\overline{\mathbf{U}}}{Dt} + \rho \frac{\partial}{\partial x_j}(\overline{u_i' u_j'}) = \rho \mathbf{g} - \nabla \overline{p} + \mu \nabla^2 \overline{\mathbf{U}} \tag{3.7}$$

This formulation has been generally referred to as the Reynolds-averaged Navier-Stokes equation and it involves a new quantity $-\rho \overline{u_i' u_j'}$ known as the Reynolds-stress tensor. These stresses are a fundamental source of difficulties within the turbulence modelling, since the turbulent inertia tensor, $\overline{u_i' u_j'}$, is never negligible in turbulent flows, yet it comprises nine new components whose analytical form is unknown in priori. In addition to the physical properties of a turbulent flow, these components

depend on local flow conditions, such as upstream history, surface roughness, geometry and velocity. Currently, no detailed knowledge of the turbulence structure exists for analytically solving the turbulent-stress tensor. However, a number of empirical approaches have been developed to address this issue. This subject is further clarified in the following Section 3.1.2, which presents the turbulence modelling technique used in this work.

3.1.2 Turbulence modelling

The previous Section 3.1.1 introduced the problematic Reynolds stress tensor that is a result from the time-averaging process and causes the main difficulties in turbulence modelling. To compute these stresses, numerous different RANS turbulence models have been developed over the time. These models can be divided to three categories based on their treatment for the stress tensor:

- Linear eddy viscosity models
- Nonlinear eddy viscosity models
- Reynolds stress models (RSM)

In this thesis, a model based on the linear eddy viscosity approach is used, and thereby the nonlinear eddy viscosity and the Reynolds stress models are not discussed here. However, for an additional information on these models, the author recommends reference [34], which provides a great review on the subject for those being interested.

The linear eddy viscosity models approximate Reynolds stresses by using the Boussinesq's hypothesis:

$$-\rho\overline{u_i'u_j'} = \mu_t\left[\left(\frac{\partial u_i}{\partial x_j}+\frac{\partial u_j}{\partial x_i}\right)-\frac{2}{3}\frac{\partial u_k}{\partial x_k}\delta_{ij}\right]-\frac{2}{3}\rho k\delta_{ij} \tag{3.8}$$

where μ_t designates the eddy viscosity, k the turbulent kinetic energy, ρ the density and δ Kronecker delta. This approximation postulates that the Reynolds stress tensor is only proportional to the strain rate tensor S_{ij}. Although this is a major simplification of the turbulent problem, it is approximately true for simple flows, such as boundary layer flows and wakes. [35]

The linear eddy viscosity models can be divided to three subcategories according to the number of equations used for solving the eddy viscosity term. The first classification is to the algebraic models that calculate eddy viscosity directly from the freestream values, thus neglecting the effects of flow history, such as convection and diffusion. The second group are the one-equation models that account one of these effects by solving an additional transport equation, which is normally for the turbulent kinetic energy. The last category comprises of two-equation models that contain second transport equation allowing them to include a history effect of diffusion. This effect is usually modelled by solving an additional turbulent variable, such as a turbulent dissipation or a specific turbulence dissipation rate, in the second transport equation. [36]

Turbulence models that are able to model the entire boundary layer, including the viscous sublayer and the buffer layer, are known as the Low Reynolds Number models. These models generally give very accurate description of the boundary layers, and can therefore be coupled with transition models. However, the Low-Re models also require high mesh resolutions leading to significantly higher computational cost compared to the models that calculate the near wall region using wall functions.

This work uses a two-equation eddy viscosity turbulence model by Menter et al. [37] that can also be utilized as a Low Reynolds Number model. Its formulation functions as the basis for the implemented transition model and is therefore described in detail in the following subsection.

Shear Stress Transport $k-\omega$ model

Shear Stress Transport turbulence model, also referred to as the SST $k-\omega$, was first introduced by Menter in 1994 [13] and has become widely used for solving engineer flow problems. Its formulation for solving turbulent eddy viscosity is based on former two-equation turbulence models; the standard $k-\epsilon$ model by Launder & Sharma [38] and the $k-\omega$ by Wilcox [39]. The principle of the Menter's model is to apply the $k-\omega$ model in the inner parts of the boundary layer and switch to the standard $k-\epsilon$ model elsewhere. As a consequence, the formulation combines the most beneficial features of both models; the $k-\omega$ model allows calculation through boundary layer all the way to the wall, and with the $k-\epsilon$ model, it avoids the Wilcox's model problems related to the inlet conditions. Hence, the SST model can be used as Low-Re turbulence model that is not overly sensitive to the inlet freestream values.

It should be noted that the OpenFOAM uses implementation of the Menter SST Two-equation Model from the year 2001 [40] with updated coefficients from [37]. The implementation has several changes compared to the original model [13], including a definition of the eddy viscosity and modified model coefficients. The two transport equations of the SST $k-\omega$ model are presented with notations according to the NASA Turbulence Modelling Resource [41]:

$$\frac{\partial(\rho k)}{\partial t}+\frac{\partial(\rho u_j k)}{\partial x_j}=P_k-E_k+\frac{\partial}{\partial x_j}\left[(\mu+\sigma_k\mu_t)\frac{\partial k}{\partial x_j}\right] \tag{3.9}$$

$$\frac{\partial(\rho \omega)}{\partial t}+\frac{\partial(\rho u_j \omega)}{\partial x_j}=\frac{\alpha}{P_\omega}\nu_t-E_\omega+\frac{\partial}{\partial x_j}\left[(\mu+\sigma_\omega\mu_t)\frac{\partial \omega}{\partial x_j}\right]+C_{d\omega} \tag{3.10}$$

where the source terms are:

$$E_k=\beta^*\rho\omega k, \qquad E_\omega=\beta\rho\omega^2$$

$$C_{d\omega}=2(1-F_1)\frac{\rho\sigma_{\omega 2}}{\omega}\frac{\partial k}{\partial x_j}\frac{\partial \omega}{\partial x_j}$$

where k is the turbulence kinetic energy and ω the spesific turbulent dissipation. The source terms consist of $C_{d\omega}$, P and E, which represent the cross-diffusion, product

and destruct terms, respectively. The switching between the models is performed by connecting the model constants with a specific blending function:

$$\phi = F_1\phi_1 + (1 - F_1)\phi_2 \tag{3.11}$$

where F_1 denotes the first blending function, ϕ_1 the inner model coefficients, ϕ_2 the outer model coefficients. The blending is possible due to the similarity of the models and due to introduction of an additional cross-diffusion term. The first blending function F_1 is zero in the freestream and becomes one inside the boundary layer and is given by

$$F_1 = \tanh\left\{\left(\min\left[\max\left(\frac{\sqrt{k}}{\beta^*\omega y}, \frac{500v}{y^2\omega}\right), \frac{4\rho\sigma_{\omega 2}k}{CD_{k\omega}y^2}\right]\right)^4\right\} \tag{3.12}$$

where the parameter $CD_{k\omega}$ is defined as:

$$CD_{k\omega} = \max\left(2\rho\sigma_{\omega 2}\frac{1}{\omega}\frac{\partial k}{\partial x_j}\frac{\partial \omega}{\partial x_j}, 10^{-10}\right) \tag{3.13}$$

After solving the transport equations (3.9) and (3.10), the turbulent eddy viscosity is computed from relation:

$$\mu_t = \frac{\rho a_1 k}{\max(a_1\omega, SF_2)} \tag{3.14}$$

in which

$$S = \sqrt{2S_{ij}S_{ij}} \tag{3.15}$$

where S defines the strain rate magnitude and F_2 the second blending function given by

$$F_2 = \tanh\left[\left[\max\left(\frac{2\sqrt{k}}{\beta^*\omega y}, \frac{500v}{y^2\omega}\right)\right]^2\right] \tag{3.16}$$

A detailed formulation for the used SST $k-\omega$ model with all the model coefficients is described in reference [37].

3.2 Discretization: Finite Volume Method

The previous Section 3.1 described the mathematical methods used in this work for modelling turbulent flows. In order to obtain numerical solutions for these modelled equations, they first need an approximation into discrete quantities. This procedure is known as the discretization, by which the underlaying mathematical model can be transformed into an algebraic system of equations. It comprises of the following elements [33]:

- **Spatial discretisation** Subdivision of the spatial domain into finite number of points, *i.e.* a creation of computational mesh.
- **Equation discretisation** PDEs are converted into a system of algebraic equations that are defined on the discretised space domain.
- **Temporal discretisation** Time domain is broken into a finite number of intervals, *i.e.* time steps Δt.

Both spatial and equation discretisation are cognate procedures determined by the chosen discretization method. However, the temporal discretisation can be considered rather a separate procedure performed by numerical schemes [33]. This work dealt only with steady state turbulent flows independent of time.

OpenFOAM software [12] is based on the Finite Volume Method, which is the most widely used technique in the computational fluid dynamics. Other often used discretization methods in CFD include the Finite Element Method (FEM), the Finite Difference Method (FDM), and the Spectral Method. However, the finite volume method distinguishes due its favorable features in CFD, such as an ease of application to arbitrary geometries and an inherent conservativity. These features originate from the method principles to directly discretize integral form of governed equations into computational domain divided into small control volumes, where cell-averaged flow quantities are stored in the cell centroid. Conversely, other methods consider a computational domain being formed by a set of discrete points.

3.2.1 Spatial discretisation

As stated before, the FVM deals with spatial discretisation by dividing the computational domain into a finite number of control volumes. In CFD, this procedure practically means creating a computational mesh with specific software that automatically defines the spatial domain. In OpenFOAM, a mesh geometry is described by a set of discrete points, also referred to as vertexes which are further used to define cell faces. The form of each cell is defined by these faces, which bound and connect the control volumes. As a result, there are no restrictions on a number of bounding faces nor face alignments. Figure 3.2 illustrates this type of cell structure that is often referred to as arbitrarily unstructured. In contrast, structured grids have prescribed face alignments and their cells are connected to each other by specific indexing system. [42]

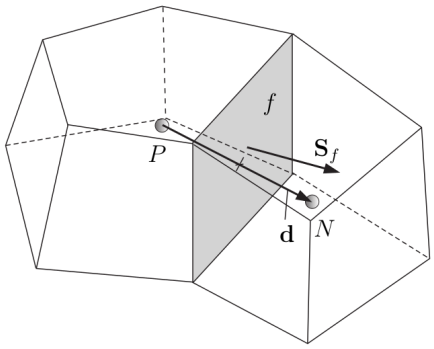

Figure 3.2: Finite-volume cell with discrete parameters [42].

In Figure 3.2, P and N represent cell-averaged values located in the cell midpoints and f denotes an internal face that connects two cells. Although, values are principally stored in cell centroids, they can also be interpolated to cell faces. For each of these internal faces, there is a designated owner cell and a neighbor cell, thus enabling a connection between adjacent control volumes. The spatial domain is divided by these cells contiguously, that is they do not overlap each other and completely fill the domain. [42]

3.2.2 Equation discretisation

Thus far, all the equations have been presented in a differential form in this paper. The principle of the FVM is to transform these equations into an integral form, which presents them as an integration over a finite volume. Next, the Gauss divergence theorem is applied in order to convert volume integrals into surface integrals. This approach grants a direct physical meaning for these conservative equations as the rate of change for variables is defined with fluxes through the volume surfaces [43]:

$$\overbrace{\frac{d}{dt}\int_V T dV}^{\text{rate of change}} = \overbrace{-\int_S \mathbf{f}(T)\cdot\mathbf{n}dS}^{\text{flow in - flow out}} \tag{3.17}$$

where T denotes any variable of density quality (*e.g.* $\rho\phi$), V the finite volume and S the control surface. $\mathbf{f}(T)$ defines the gross flux of T over the control volume faces S, that is the total difference between the inflow and outflow fluxes. The following expression is derived by expressing integration as direct summation over the discretised spatial domain:

$$\frac{d}{dt}(T_i V_i) = -\sum_j \mathbf{f}(T_j)\cdot\mathbf{n_j}dS \tag{3.18}$$

where V_i signifies a single volume element of the mesh bounded by its surfaces S_j. This type of approach automatically satisfies the conservation law since the basic

flow quantities, such as mass, momentum and energy do not vanish in the discrete equations.

For instance, consider a general form of transport equation:

$$\frac{\partial \rho\phi}{\partial t} + \nabla \cdot (\rho \mathbf{U}\phi) = \nabla \cdot (\alpha \nabla \phi) + Q_\phi \tag{3.19}$$

where α refers to the diffusion coefficient, ρ the density, ϕ any scalar variable and Q_ϕ the source term. As the FVM uses integral forms, the transport equation is next integrated over a control volume:

$$\overbrace{\int_V \frac{\partial \rho\phi}{\partial t} dV}^{\text{time derivate}} + \overbrace{\int_V \nabla \cdot (\rho \mathbf{U}\phi) dV}^{\text{convection term}} = \overbrace{\int_V \nabla \cdot (\alpha \nabla \phi) dV}^{\text{Laplacian term}} + \overbrace{\int_V Q_\phi dV}^{\text{source term}} \tag{3.20}$$

The components of a PDE differ in mathematical characteristics, thus require a dissimilar treatment in a discretisation process. The derivative terms can be approximated from a discrete domain using optional numerical methods referred to as numerical schemes within CFD. These numerical schemes play an important role in the discretization process since they have a major impact on the solution. Therefore, the following Section 3.3 provides a more close description of the numerical schemes involved in this work.

With the finite-volume method, the time derivative term is directly treated with the chosen numerical scheme whereas the spatial terms (convection and Laplacian) are first converted to surface integrals by applying the Gauss divergence theorem. The source term is simply multiplied by a discrete volume. The discrete form is obtained when integrals are presented as sum of discrete quantities:

$$\overbrace{\frac{\partial \rho\phi}{\partial t} V_i}^{\text{time derivate}} = \overbrace{-\sum_f \mathbf{S_f} \cdot (\rho \mathbf{U})_f \phi_f}^{\text{convection term}} + \overbrace{\sum_f \alpha_f \mathbf{S_f} \cdot (\nabla \phi)_f}^{\text{Laplacian term}} + \overbrace{Q_\phi V_i}^{\text{source term}} \tag{3.21}$$

where $\mathbf{S_f}$ refers to the surface area vectors that bound the control volume V_i. It is important to note that this formulation defines multiple values on control volume faces, subscribed with f, due to application of the Gauss divergence theorem. As a consequence, these variables require an interpolation to the cell faces, which is also realized using numerical schemes. [42]

3.3 Numerical schemes

Numerical schemes are algorithms that approximate a numerical solution for problems related with PDEs and have a crucial role in the discretization phase. They express continuous derivatives as well as interpolate values with a finite number of discrete points from the computational domain. Not only do the numerical schemes connect a solution of a single control volume to its adjacent cells, they have a significant effect on the stability as well as on the numerical accuracy of the entire solution.

The stability signifies that a numerical error remains sufficiently low in each grid point, thus not affecting the solution. For instance, in a case of instability, the error grows during iteration rounds eventually leading to a breakdown of the entire calculation. A solution always contains some numerical error which consists of a truncation and a rounding error [43]. The truncation error results when a continuous problem is approximated with a finite number of points. Therefore, applied schemes should be as high-order as possible in order to minimize this numerical error. A rounding error arises as digital computer reserves a finite amount of memory for each number, thus not calculating with exact real numbers. However, this error is usually negligible compared to the truncation error [43].

Normally, each component of the PDE is discretized with a different numerical scheme given to their dissimilar mathematical nature. For instance, Laplacian terms are diffusive and should be treated with a second order central difference scheme during the discretisation [33]. Table 3.1 presents the numerical schemes applied in this work. This same representation is also used in the OpenFOAM software, which allows the user to manually select a discretisation method for each individual component. [42]

Table 3.1: The numerical schemes applied in the simulations

Term	Mathematical expression	Numerical Scheme
Time derivative	$\partial/\partial t$	steadyState
Gradient	$\nabla\phi$	central differencing
Laplacian	$\nabla^2\phi$	central differencing
Divergence	$\nabla\cdot(\psi)$	high-resolution 2nd order

Generally, time independent flows can be simulated with either a steady-state or a transient approach depending on the solver. This work applies the first approach, in which the time derivatives are simply set to equal zero (*steadyState* scheme). The other option is normally referred to as the time marching where a transient simulation is proceeded until the solution does not change with respect to time.

Gradient and Laplacian terms are approximated using a central differencing method that is also referred to as the linear interpolation. This is actually a finite difference discretization method derived through Taylor series expansion, however, also applicable in FVM. For instance, the following equation presents a gradient approximated with a symmetrical differencing in a one-dimensional case with a structured mesh [43]:

$$\nabla\phi_i = \frac{\phi_{i+1} - \phi_{i-1}}{2\Delta x} + O(\Delta x^2) \tag{3.22}$$

where Δx denotes the distance between the cell centroids and $O(\Delta x^2)$ the truncation error of second order. This error causes oscillating behaviour in the solution, and thereby the scheme is not applicable to all terms (*e.g.* convection term). However, first-order upwind schemes do not include this behaviour, instead, are inherently monotone. Furthermore, they take the flow direction into account, thereby being suitable for representing the physical nature of a fluid flow:

$$\phi_{f_e} = \begin{cases} \phi_P, & \mathbf{S} \cdot \mathbf{U} \geq 0 \\ \phi_E, & \mathbf{S} \cdot \mathbf{U} < 0 \end{cases} \tag{3.23}$$

where P signifies the cell in question and E the control volume to east. Although the first-order upwind schemes are usually too inaccurate to be applied in practical fluid simulations, the concept itself is essential in CFD as numerous more advanced algorithms are based on it. For instance, consider an interpolation to cell face:

$$\phi_{f_e} = \phi_P + (\nabla\phi)_P \cdot \Delta\mathbf{r} \tag{3.24}$$

where $\Delta\mathbf{r}$ defines the distance vector from centroid P to the face. Applying equation (3.22) together with equation (3.23) on the gradient term $(\nabla\phi)_P$ yields a second-order upwind scheme.

The treatment of divergence terms, $\nabla\cdot$, is the most crucial part to be considered when selecting numerical schemes. This is due to the inclusion of advection terms that are hyperbolical in nature, and whose numerical treatment has been posing a major challenge for decades within CFD. For transitional computations, Langtry [44] recommends high-resolution bounded second order schemes as a default setting. The high-resolution concept aims to preserve monotonicity by controlling numerical fluxes with nonlinear limiter functions while still achieving at least second order accuracy. The concept was initially introduced by two separate authors Van Leer [45] and Boris & Book [46] in 1973, and has since yielded a number of different approaches.

One of the most used applications are Total Variation Diminishing (TVD) schemes that limit numerical fluxes. Their general presentation can be written as a blending between first order (UD) and higher order (HO) schemes [47]:

$$\phi_{f_e} = (\phi)_{UD} + \Psi(r)[(\phi)_{HO} - (\phi)_{UD}] \tag{3.25}$$

where $\Psi(r)$ represents the limiter function dependent on the ratio of successive gradients:

$$r = \left(\frac{\phi_P - \phi_W}{\phi_E - \phi_P} \right) \tag{3.26}$$

Requirements for schemes to be TVD, introduced by Sweby [48], are defined by the $\Psi(r) - r$ relationship. These constraints color the shaded region in Figure 3.3, which also presents the limiter, *limitedLinear*, used in this work. In addition, to demonstrate other options available, Figure 3.3 includes two widely utilized limiter functions: Van Leer [49] and SUPERBEE [50].

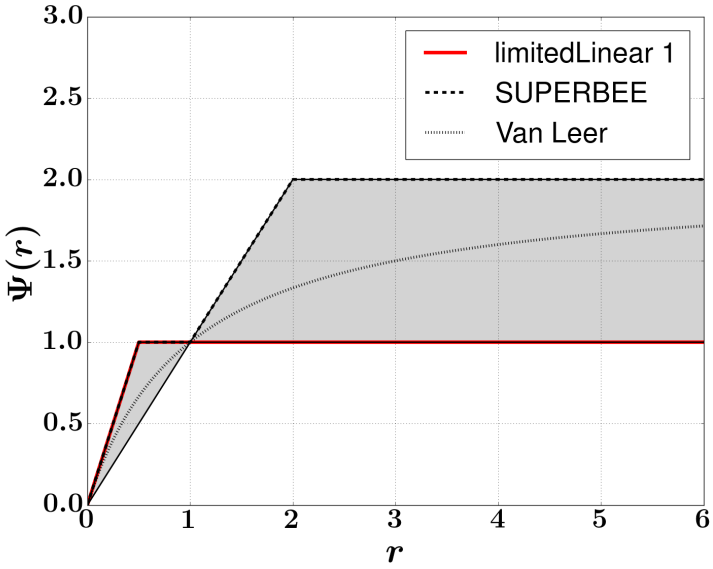

Figure 3.3: Limiters for high-resolution schemes.

In this thesis, the velocity convection term (divρU) was discretized with a bounded second-order upwind-biased scheme applying a V-limiter (*linearUpwindV*) in order to ensure solution stability. The remaining convection terms for the turbulent variables were discretised using an OpenFOAM specific TVD scheme *limitedLinear 1*, shown in Figure 3.3, that is based on the central differencing and limits towards the upwind in regions where gradients change most rapidly. It should be noted that this limiter function requires a coefficient (from 0 to 1) with 1 being the strongest limiting towards upwind. In addition, a bounded variant of this scheme was applied as it is the recommended setup for incompressible steady-state cases [51].

3.4 Solution algorithm: SIMPLE

As a result of the discretisation phase, the governing formulae are now transformed into an algebraic system of equations. To provide an efficient resolution for this set of equations, a wide variety of methods have been developed over time. These methods are commonly referred to as the solution algorithms that aim to resolve the set of algebraic equations while trying to obtain a high accuracy and a fast convergence. The algorithms can be divided to two groups based on their approach: direct and iterative methods. Generally, the more efficient direct methods are only applicable on specific linear problems, such as a resolution of tridiagonal matrices, whereas the iterative methods are used elsewhere due to nonlinear characteristics and a high-resolution mesh requirements of the fluid problems. A suitable solution algorithm for a specific simulation naturally depends on the flow characteristics, such as time dependency and compressibility.

A resolution of incompressible flows, such as in this work, pose a difficulty known as the pressure-momentum coupling problem. This problem occurs since the conti-

nuity equation is not connected to the solution due to the absence of pressure terms. As a consequence, an incompressible problem includes only three equations (momentum) for solving four unknowns (one pressure and three velocity terms). Techniques that connect the pressure to the continuity equation are generally referred to as the pressure correction or pressure-based methods. In this approach, the pressure is expressed with a special equation derived using the continuity equation (2.4) in conjunction with the momentum equation (2.8). The idea is to take a divergence from the incompressible momentum equations:

$$\nabla \cdot \mathbf{M} = \frac{\partial}{\partial x} M_x + \frac{\partial}{\partial y} M_y \tag{3.27}$$

where $\mathbf{M}$ represents the incompressible momentum equations written in vector form. Applying the continuity ($\nabla \cdot \mathbf{U}$) principle and re-arranging the terms results in a pressure correction in respect of the mass conservation principle:

$$\frac{1}{\rho} \nabla^2 p = -\nabla \cdot (\mathbf{U} \cdot \nabla)\mathbf{U} \tag{3.28}$$

This equation (3.28) is commonly known as the Poisson equation for pressure, in which the change of pressure, Δp, is expressed in terms of velocities $\mathbf{U}$. The pressure correction methods are based on an iterative process that proceeds in steps for solving segregated equations. The fundamental is to first apply initial values into the discretised equations for obtaining intermediate values. Next, these values are updated through consecutive steps of corrections in order to satisfy the mass conservation principle. Finally, the initial values are substituted with the corrected ones, and the entire process is repeated until sufficient convergence is reached.

Over the time, a variety of pressure correction methods have been developed for different flow conditions. This work applies the renowned Semi-Implicit Pressure Linked Equations (SIMPLE) solution algorithm by Patankar and Spalding [52]. OpenFOAM recommends this algorithm for incompressible steady-state flows, whereas suggests transient flows to be solved using either the Pressure Implicit with Splitting of Operators (PISO) by Issa [53] or a combination of the two aforementioned methods referred to as the PIMPLE algorithm [51].

The following Figure 3.4 illustrates the operating procedure of a conventional SIMPLE algorithm [54]. Although the SIMPLE algorithm is implemented into the OpenFOAM source code somewhat differently, it follows the same principles as demonstrated in Figure 3.4. First, the discretized momentum equations are solved using either initial values or old values from previous rounds resulting in an intermediate velocity field $\mathbf{U}^*$. Next, this approximated velocity field is substituted into the pressure correction equation to attain the correction term p', which is further used to correct the pressure and velocity variables. In the step four, remaining transport equations are resolved with the corrected values from previous step. Finally, initial values and boundary conditions are updated with the new values, and the whole process is repeated until sufficient convergence is achieved. It should be noted that all the new values, including the scalar variables ϕ, are obtained using under-relaxation factors for avoiding a possible divergence of a solution. [54]

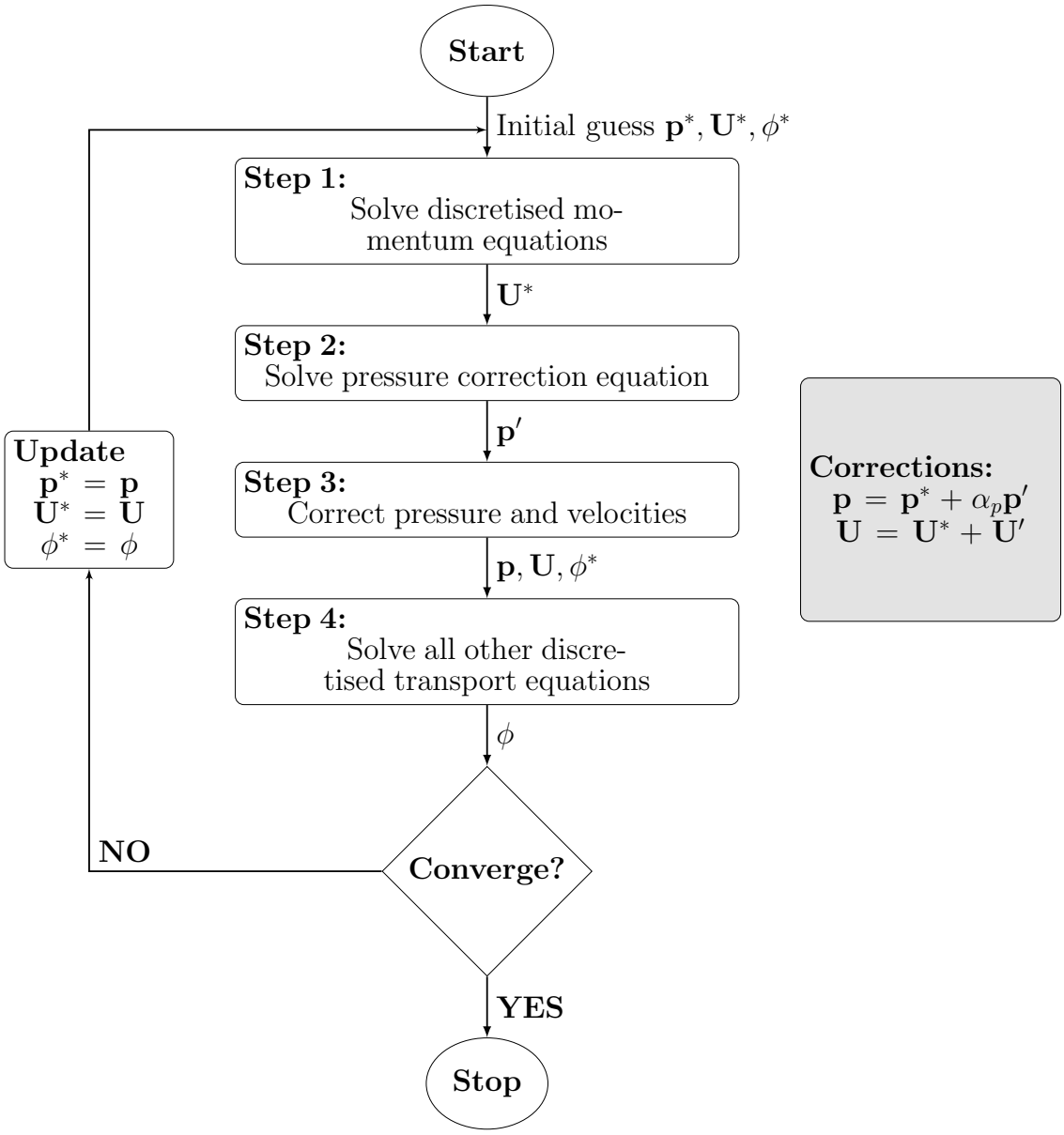

Figure 3.4: The SIMPLE algorithm.

3.5 Post-processing

The term post-processing refers to all the means for managing as well as visualizing a vast amount of numerical data obtained from simulations. The post-processing phase is an important part of a simulation process as it enables the examination of numerical results through data extraction and visualization, which helps to distinguish the desired features of the flow. However, it should be emphasized that an incorrect handling of data in the post-processing phase can lead to erroneous conclusions, although the actual simulation could have been correctly constructed.

Generally, all commercial CFD softwares have inbuilt post-processing tools that allow processing and graphical presentation of simulation data. OpenFOAM provides a user with a number of inbuilt post-processing functions for processing numerical data, and includes an open-source third-party application *paraFoam* for flow visualization. In addition to these tools, this work utilized a customized *python* code and the *gnuplot* for requisite graphical plotting of the data. All the post-processing tools involved in this work are specified in tables 3.2 and 3.3.

Table 3.2: Data processing tools

OpenFOAM functions	Object
foamLog	extracts residuals from log-files
wallShearStress	calculates wall shear stresses
yPlus	calculates y^+ values
sampleDict	extracts variables along predetermined paths

Table 3.3: Visualization tools

Program	Object
paraFoam	Scalar and vector fields
gnuplot	Residuals
python	2D plotting

Chapter 4

Transition Modelling

The previous Chapter 3 introduced the fundamentals of the turbulence modelling with RANS methods used for approximating the physics of turbulent flow. The problem is that all conventional turbulence models inherently consider the entire boundary flow as turbulent and are thereby unable to include the laminar flow region and the transition process into calculations. To remove this deficiency, numerous studies have focused on the development of transition models for including this important phenomenon into RANS simulations. Although some transition models are able to predict transition accurately, they only tend to achieve this under specific conditions which cannot be reliably applied to general flow problems. Moreover, transition models often rest on a complex formulation that hinders the model implementation and fine-tuning for varying flow cases.

This chapter introduces the current approaches for the transition modelling, focusing on a one-equation LCTM model [1] that appears as a promising option for predicting a transition within common engineering flow problems. The section 4.1 provides a brief description of the most commonly used transition modelling techniques. The section 4.2 introduces the operational principles of the γ-model as well as defines the model formulation and the coupling with the SST $k-\omega$ turbulence model. The final section provides a brief introduction for programming in the OpenFOAM followed by a detailed description of the gamma model implementation into versions 4.x of OpenFOAM.

4.1 Current modelling methods

An explicit categorization of transition models is rather difficult as models commonly combine multiple features of different characteristics. Therefore, this thesis does not aim to provide a precise classification for them, but rather shows individual concepts and points out single transition prediction models that have been widely utilized. Although a transition can also be modelled using the LES and DNS methods, they are not comparable with shown methods due to their high requirements for computational power, thus being out of the scope of this thesis.

Low-Reynolds-Number turbulence models

Many Low-Re turbulence models have been observed to generate results that mimic the transition phenomenon. Although some models have produced qualitative results under specific conditions, no model has been able to generate reliable results in varied flow conditions. The ability is merely a consequence of similar mathematical properties within turbulence equations and is not based on actual experimental correlations. Hence, these models are not generally suitable for transition prediction. [8]

e^N method

The e^N method is based on the local linear stability theory and predicts a transition by calculating the growth of disturbance amplitudes within the boundary layer flow. The technique was developed independently by two authors in 1956: Van Ingen [55], and Smith and Gamberoni [56]. It has been shown that the method is able to approximate the onset of transition for isolated airfoils with excellent accuracy. Hence, the e^N technique has become the most widely utilized transition prediction technique within the aircraft industry [44].

However, the e^N method contains a major deficiency as it requires information from the initial interference amplitudes within the layer in order to be calibrated. This quality is dependent on the troublesome flow receptivity process, a somewhat unique feature for each flow case, and therefore requires experimental tests to be determined for dissimilar cases. Hence, the e^N is referred to as a semi-empirical method due to need for experimental data in order to achieve reliable transition predictions. [44]

Intermittency models

A number of models predict a transition by solving a variable known as the intermittency factor. This term represents the level of turbulence in the flow defined by the ratio of time in which the flow is turbulent at given point within a boundary layer. For instance, with value of zero, it describes a laminar flow whereas an intermittency factor of value 0.5 ($\gamma = 0.5$) denotes that the flow is 50 percent of the time turbulent.

Over the years, numerous models that base on solving the intermittency factor have been proposed. They can be categorized to algebraic and intermittency transport models depending on the technique used for resolving the intermittency factor [44]. The fundamental idea of this approach is to control the transition by coupling the source terms of the underlaying turbulence model with the intermittency factor, whose formulation often relies solely on empirical correlations. Consequently, the intermittency models are not able to solve the actual physics behind the transition, but require correlations obtained from another model, such as an experimental correlation. As a redeeming feature, intermittency models can be extended to include non-linear effects, such as crossflow and surface roughness.

The most renowned representative of this approach is the local correlation-based $\gamma - Re_{\theta t}$ intermittency transport model by Langtry [44], which has proven a good overall function in transition prediction [8]. In addition, the model has been extended to include the effects of crossflow and surface roughness that were studied, for instance, in the recent work by Kruljevic [15].

Laminar kinetic energy models

Recently, much research has been directed toward modeling of the laminar-turbulence transition using the physics-based laminar kinetic energy models. The technique is based on RANS method, however, it includes an additional transport equation for describing the kinetic energy of laminar fluctuations within a pre-transitional boundary layer. The idea is that sufficiently high levels of laminar kinetic energy trigger the turbulence production in the underlaying turbulence model, thereby controlling the onset of the transition.

This concept was first introduced by Mayle and Schultz [57] and has since been used in several transition models [3, 4, 6]. In general, these models have been observed to generate good results in varying flow conditions and are promising options for transition modelling. For instance, the three-equation eddy-viscosity model by Walters and Cokljat [3], whose formulation is given below as an example of this approach, has achieved much popularity over recent years.

$$\frac{Dk_t}{Dt} = P_{k_T} + R_{BP} + R_{NAT} - \omega k_T - D_T + \frac{\partial}{\partial x_j}\left[\left(\nu + \frac{\alpha_T}{\sigma_k}\right)\frac{\partial k_T}{\partial x_j}\right] \tag{4.1}$$

$$\frac{Dk_L}{Dt} = P_{k_L} - R_{RB} - R_{NAT} - D_L + \frac{\partial}{\partial x_j}\left[\nu\frac{\partial k_L}{\partial x_j}\right] \tag{4.2}$$

$$\begin{aligned}\frac{D\omega}{Dt} &= C_{\omega 1}\frac{\omega}{k_T}P_{k_T} + \left(\frac{C_{\omega R}}{f_W} - 1\right)\frac{\omega}{k_T}(R_{BP} + R_{NAT}) - C_{\omega 2}\omega^2 \\ &\quad + C_{\omega 3} f_\omega \alpha_T f_W^2 \frac{\sqrt{k_T}}{d^3} + \frac{\partial}{\partial x_j}\left[\left(\nu + \frac{\alpha_T}{\sigma_k}\right)\frac{\partial \omega}{\partial x_j}\right]\end{aligned} \tag{4.3}$$

4.2 One-Equation Local Correlation-based Transition Model

The One-equation Local Correlation-based Transition Model, also referred to as the γ-model, predicts transition by solving a single transport equation for intermittency that depends on local variables. The model was first introduced by Menter et al. in 2015 [1], and it can be considered as a new, enhanced version of the widely used Langtry-Menter $\gamma - Re_\theta$ model originally published in 2006 [44]. The γ-model entails some beneficial features including a simplified formulation and an improved execution of the Local Correlation-based Transition Model (LCTM) concept compared to the prior model.

The basic idea of the γ-model is to influence the turbulence kinetic energy production of the underlaying turbulence model by coupling its source terms with an intermittency factor, which represents the level of turbulence in the flow. The intermittency is solved from a standard convection-diffusion transport equation determined by empirical correlations that are formulated solely using local variables [1]. Consequently, the model is Galilean invariant, which is an advantageous feature in CFD simulation since it allows the movement of walls with respect to the coordinate system. Furthermore, the model follows the LCTM concept enjoying its perquisites.

The Local Correlation-Based Transition Modelling concept was first introduced by Menter et al. in 2002 [58], and its framework relies on experimental correlations that depend on local variables. The technique is to integrate these correlations into standard convection-diffusion transport equations principally through triggering functions that initiate the process of transition. It is important to notice that within LCTM concept, there is no attempt to model the actual physics behind laminar-turbulence transition processes. Instead, the aim is to formulate CFD-compatible transport equations that enable the combination of local experimental correlations. The motive behind this kind of approach is to provide a transition model with a generic composition for allowing it to be coupled with other turbulence models. In addition, the generic form enables the further inclusion of virtually any transitional effect provided with a sufficient amount of experimental information. [1]

The gamma model offers a number of advantages compared to the prior transition model. First, the reduced number of transport equations simplifies the model notably compared to the original version that contains an additional transport equation for transition onset momentum thickness. Second, it uses only local variables in correlations rendering the model Galilean invariant, contrary to the $\gamma - Re_\theta$ model, where the turbulence intensity, Tu, is a freestream variable preventing the model of being Galilean invariant. Finally, due to straightforward formulation, the model succeeds to provide more meaningful constants, thereby easing its adjustment to varying flow cases.

4.2.1 Model formulation

Transport equation for intermittency

The transition model is coupled with the turbulence model with the intermittency factor, γ, that is defined as a zero ($\gamma = 0$) in the freestream and reaches its maximum value of one ($\gamma = 1$) at a state of full turbulence. The boundary conditions for intermittency are defined following way: a normal flux equals one at the inlet ($\dot{\mathbf{m}}\gamma \cdot \mathbf{n} = 1$) and equals zero at the wall ($\dot{m}\gamma \cdot \mathbf{n} = 1$). It should be noted that the intermittency is also set to equal one ($\gamma = 1$) in the freestream, although it should have zero values from physical point of view, however, this approach has several advantages for calculations especially within stagnation regions as well as within regions close to boundary layer edge. The distribution of γ is determined using a generic transport equation:

$$\frac{\partial(\rho\gamma)}{\partial t} + \frac{\partial(\rho U_j \gamma)}{\partial x_j} = P_\gamma - E_\gamma + \frac{\partial}{\partial x_j}\left[\left(\mu_t + \frac{\mu_t}{\sigma_\gamma}\right)\frac{\partial \gamma}{\partial x_j}\right] \tag{4.4}$$

This type of formulation allows to include the time history of the variable, which is essential considering the nature of the transition phenomenon. In equation (4.4), terms μ_t, μ and ρ denote the eddy viscosity, the kinematic viscosity and the density, respectively. The destruction term E_γ takes into account a possible flow relaminarization under the influence of highly favorable pressure gradients and is given by:

$$E_\gamma = c_{a2}\rho\Omega\gamma F_{turb}(c_{e2}\gamma - 1) \tag{4.5}$$

where Ω is the magnitude of the absolute vorticity rate and F_{turb} the transition control function of the model. P_γ is the transition source term, which is set by the models design criteria to equal zero in the laminar boundary layer upstream of transition and to activate at the point of transition according to the onset criteria depending on the local correlations. It is defined by the following equation:

$$P_\gamma = F_{length}\rho S\gamma(1-\gamma)F_{onset} \tag{4.6}$$

where S is the strain rate magnitude and F_{length} a model constant, which determines the magnitude of this source term. F_{onset} is an activate source term that triggers the intermittency production in the model. The transition model becomes active only within the boundary layer region, and thereby does not interfere the freestream turbulence production controlled by the underlaying turbulence model. It consists of a number of sub-functions that depend on local correlations and model constants:

$$F_{onset} = \max[F_{onset2} - F_{onset3}, 0] \tag{4.7}$$

$$F_{onset1} = \frac{Re_v}{2.2 Re_{\theta c}} \tag{4.8}$$

$$F_{onset2} = \min[F_{onset1}, 2.0] \tag{4.9}$$

$$F_{onset3} = \max\left[1 - \left(\frac{R_T}{3.5}\right)^3, 0\right] \tag{4.10}$$

$$F_{turb} = e^{-(\frac{R_T}{2})^4} \tag{4.11}$$

$$R_T = \frac{\rho k}{\mu \omega} \tag{4.12}$$

$$Re_v = \frac{\rho d_w^2 S}{\mu} \tag{4.13}$$

$$Re_{\theta c} = f(Tu_L, \lambda_{\theta L}) \tag{4.14}$$

The model constants are:

$$F_{length} = 100, \qquad c_{e2} = 50, \qquad c_{a2} = 0.06, \qquad \sigma_\gamma = 1.0 \tag{4.15}$$

where d_w is the wall distance, μ the kinematic viscosity, ω the specific turbulence dissipation rate, and k the turbulence kinetic energy. The local vorticity Reynolds number Re_v, also known as the strain-rate Reynolds number, forms a ratio with the critical Reynolds number $Re_{\theta c}$ that has an eminent role in on-setting the intermittency production within the equation (4.8). Furthermore, it is important to note that the strain rate magnitude S is the driving force behind transition. It appears in the source term and local Re_v formulations in equations (4.6) and (4.13).

Local formulations for Tu_L and $\lambda_{\theta L}$

The correlation is based on two variables: the local turbulence intensity Tu_L and the local pressure gradient $\lambda_{\theta L}$. These variables are used for approximating the critical Reynolds number $Re_{\theta c}$, which is defined in equation (4.14). Contrary to the prior model, both of these arguments are approximated using strictly local variables. Not only does this remove the need for a second transport equation, it also allows the model to achieve Galilean invariancy since no global arguments remain in the formulation. The local turbulence intensity is presented in percents and given by

$$Tu_L = \min\left(100\frac{\sqrt{2k/3}}{\omega d_w}, 100\right) \tag{4.16}$$

where k is the turbulence kinetic energy, d_w the wall distance and ω the specific turbulence dissipation rate. The usage of the freestream velocity U is avoided with the following approximation:

$$U \sim S d_w \sim \omega d_w \tag{4.17}$$

where S is the strain rate magnitude. Menter proposes this type of formulation to have an additional advantage since the turbulence modes that do not model the specific turbulence dissipation rate, ω, can utilize the relation $\omega \approx S/0.3$.

The local pressure gradient parameter $\lambda_{\theta L}$ is expressed as:

$$\lambda_{\theta L} = -7.57 \cdot 10^{-3} \frac{dV}{dy} \frac{d_w^2}{\nu} + 0.0128 \tag{4.18}$$

where ν designates the kinematic viscosity and d_w the distance from the wall. dV/dy is the wall-normal velocity gradient, in which V is the wall-normal velocity and y the normal-to-wall coordinate in the freestream. For a general geometry case, Menter suggests this term to be computed with the following equation:

$$\frac{dV}{dy} \equiv \nabla(\mathbf{n} \cdot \mathbf{U}) \cdot \mathbf{n} \tag{4.19}$$

It should be noted that equation (4.18) is based on the definition for pressure gradient parameter on flat plate that yields from two-dimensional considerations:

$$\lambda_\theta = \frac{\rho\theta^2}{\mu} \frac{dU}{dx} = -\frac{\rho\theta^2}{\mu} \frac{dV}{dy} \tag{4.20}$$

Consequently, the transition model fails to include the effects induced by a three-dimensional phenomena, such as a crossflow. Moreover, equation (4.20) is not valid inside the boundary layer in which the pressure remains constant. However, here the velocity gradient dV/dy is utilized rather as an indicator for imposed freestream pressure gradients.

The local approximation for the pressure term was achieved by replacing the momentum thickness of the equation (4.20) with the wall distance d_w. This is possible since the transition model is activated near the boundary layer center, where the following correlation provides sufficient accuracy:

$$d_w = \frac{\delta_{99\%}}{2} \sim \theta \tag{4.21}$$

in which $\delta_{99\%}$ refers to the boundary layer thickness. The scaling coefficients of equation (4.18) were obtained through calibration against a variety of Falker-Skan profiles and the purpose of constant 0.0128, is to capture the non-zero essence of the velocity gradient in zero pressure gradient flows.

To maintain numerical robustness, the pressure gradient parameter $\lambda_{\theta L}$ is restricted with the following boundaries:

$$\lambda_{\theta L} = \min(\max(\lambda_{\theta L}, -1.0), 1.0) \tag{4.22}$$

4.2.2 Correlations

The correlation for the critical Reynolds number, $Re_{\theta c}$, is composed of several arguments: two local variables, three model parameters and a model correlation function.

$$Re_{\theta c}(Tu_L, \lambda_{\theta L}) = C_{TU1} + C_{TU2} \exp[-C_{TU3} Tu_L F_{PG}(\lambda_{\theta L})] \tag{4.23}$$

Model parameters are:

$$C_{TU1} = 100.0, \qquad C_{TU2} = 1000.0, \qquad C_{TU3} = 1.0 \tag{4.24}$$

where Tu_L is the local turbulence intensity and F_{PG} the model correlation function. The formulation itself is rather straightforward and the constant model parameters are more accessible for modifications than in the prior transition model. The first parameter C_{TU1} specifies the minimum value for $Re_{\theta c}$. This is required as the exponent approaches zero, while the local turbulence Tu_L gains high values. The equation reaches its maximum values when Tu_L approaches zero levels, thus the sum of $C_{TU1} + C_{TU1}$ defines the maximum value for $Re_{\theta c}$. Parameter C_{TU3} inside the exponent controls the rate of change of turbulence intensity.

Formulation includes the correlation function F_{PG}, which is intended to account the influence of streamwise pressure gradient:

$$F_{PG}(\lambda_{\theta L}) = \begin{cases} \min(1 + C_{PG1}\lambda_{\theta L}, C_{PG1}^{\lim}), \lambda_{\theta L} \geq 0 \\ \min(1 + C_{PG2}\lambda_{\theta L} + C_{PG3}\min[\lambda_{\theta L} + 0.0681, 0], C_{PG2}^{\lim}), \lambda_{\theta L} < 0 \end{cases} \tag{4.25}$$

The function parameters are:

$$C_{PG1} = 14.68, \qquad C_{PG2} = -7.34, \qquad C_{PG3} = 0.0 \tag{4.26}$$

$$C_{PG1}^{\lim} = 1.5, \qquad C_{PG2}^{\lim} = 3.0 \tag{4.27}$$

It is important to note that the F_{PG} function is required to correct the $Re_{\theta c}$ values in cases where the local turbulence intensity Tu_L is non-zero. When Tu_L is zero the $Re_{\theta c}$ becomes totally independent of $\lambda_{\theta L}$. In addition, the function is entirely empirical in nature since it is adjusted to fit the experimental results. In procedure to accomplish this goal, the function parameters were calibrated against wide range of Falkner-Skan flows.

4.2.3 Coupling with the turbulence model

In this thesis the gamma transition model is coupled with the SST $k - \omega$ turbulence model using the approach presented in the original paper by Menter [1]. The technique is to connect the intermittency factor to the transport equation of the turbulent kinetic energy by coupling it with the source and destruction terms. The modified turbulence equations are presented as follows:

$$\begin{aligned} \frac{\partial}{\partial t}(\rho k) + \frac{\partial}{\partial x_j}(\rho u_j k) &= \tilde{P}_k + P_k^{\lim} - \tilde{D}_k + \frac{\partial}{\partial x_j}\left((\mu + \sigma_k \mu_t)\frac{\partial k}{\partial x_j}\right) \\ \frac{\partial}{\partial t}(\rho\omega) + \frac{\partial}{\partial x_j}(\rho u_j \omega) &= \alpha\frac{P_k}{v_t} - D_\omega + Cd_\omega + \frac{\partial}{\partial x_j}\left((\mu + \sigma_\omega \mu_t)\frac{\partial \omega}{\partial x_j}\right) \end{aligned} \tag{4.28}$$

where $\tilde{P}_k$ and $\tilde{D}_k$ are the modified production and the destruction terms, respectively, and are defined as follows:

$$\tilde{P}_k = \gamma P_k \tag{4.29}$$

$$\tilde{D}_k = \max(\gamma, 0.1) D_k \tag{4.30}$$

where γ denotes the intermittency factor. Terms P_k and D_k are the production and the destruction terms of the original SST $k-\omega$ model, respectively. Equation (4.28) includes an additional production term P_k^{lim} whose purpose is to generate turbulence kinetic energy under certain circumstances. It is necessary in conditions where turbulent intensity diminishes towards very low and zero values. The term ensures proper activation of k since the underlaying SST $k-\omega$ turbulence model fails to generate sufficiently turbulent kinetic energy inside the boundary layer on low Tu levels. Once the fully turbulent state of the boundary layer has been met, P_k^{lim} turns itself off automatically. This additional source term is:

$$P_k^{\text{lim}} = 5C_k \max(\gamma - 0.2, 0)(1-\gamma)F_{on}^{lim} \max(3C_{SEP}\mu - \mu_t, 0)S\Omega \tag{4.31}$$

$$F_{on}^{\text{lim}} = \min(\max\left(\frac{Re_V}{2.2 \cdot Re_{\theta c}^{\text{lim}}} - 1, 0\right), 3) \tag{4.32}$$

$$Re_{\theta c}^{\text{lim}} = 1100 \tag{4.33}$$

where S denotes the strain rate magnitude, Ω the absolute vorticity rate magnitude, Re_V local vorticity Reynolds number and the variables μ and μ_t are the dynamic and the eddy viscosity, respectively. The model constants C_k and C_{SEP} are set to values:

$$C_k = 1.0, \qquad C_{SEP} = 1.0 \tag{4.34}$$

The formulation can be readily interpreted when it is divided in parts: the first section $\max(\gamma - 0.2, 0)$ restrains the source term from activating before the transition model, the second part $\max(3C_{SEP}\mu - \mu_t, 0)$ is responsible for switching off in fully turbulent state and the F_{on}^{lim} function ensures that the additional source term is active only for high Reynolds numbers and/or separating flows. The given constants have practical significance as C_{SEP} controls the size of separation bubble, $Re_{\theta c}^{\text{lim}}$ sets the limits for Reynolds number and flow separation, and with C_k it is possible to adjust the source term magnitude from its default value.

The blending function of the turbulence model needs to be modified:

$$R_y = \frac{\rho y \sqrt{k}}{\mu}, \qquad F_3 = e^{-\left(\frac{R_y}{120}\right)^8}, \qquad F_1 = \max(F_{1orig}, F_3) \tag{4.35}$$

where F_{1orig} refers to the blending function from the unaltered SST $k-\omega$ turbulence model. The modified formulation is the same as used in the previous $\gamma - Re_\theta$ model. This modification secures that F_1 invariably equals to 1.0 in laminar boundary layer. Consequently, the $k-\omega$ model is active throughout near-wall regions.

4.3 OpenFOAM implementation

This section provides a brief introduction on programming within OpenFOAM followed by a "step-by-step" tutorial of the transition model implementation applicable for OpenFOAM 4.x. versions in the Linux environment.

4.3.1 Programming in OpenFOAM

OpenFOAM [12] is a free open source CFD software, *i.e.* the source code is entirely available for all users to access. The source code itself is based on the object-oriented C++ language, which has various beneficial features for CFD programming. The class based architecture allows effective use of abstraction, modularity and data structures. Furthermore, the template meta-programming technique avoids a code duplication, thus minimizes its size. The C++ libraries contain a great number of mathematical instruments, solvers, models and applications that can be accessed and customized according to the user needs. The OpenFOAM directory structure is divided to four main directories listed below [59]:

- **src:** the core OpenFOAM libraries
- **applications:** solvers and utilities
- **tutorials:** tutorial test-cases
- **doc:** documentation

OpenFOAM approaches the continuum mechanical problems by representing the spatial dimensions in the Cartesian coordinate system and describing the physical entities with tensors. This is convenient as any scalar or vector, in addition to tensor itself, may be presented as a tensor and linked to the coordinate system with the index notation. The basic tensor classes with their access functions are represented in table 4.1.

Table 4.1: Tensor classes in OpenFOAM [42].

Rank	Common name	Basic class	Access functions
0	Scalar	scalar	
1	Vector	vector	$x(), y(), z()$
2	Tensor	tensor	$xx(), xy(), xz()...$

The software deals with the tensor calculations by using algebraic operations, for which a large number of different functions are available. The syntax for these operations is identical to the common mathematical notations in most cases. Table 4.2 presents operations to rank 2 tensors, from which some of are also required in the transition model implementation. [42]

Table 4.2: Operations to rank 2 tensors [42].

Operation	Mathematical description	Description in OpenFOAM
Transpose	$\mathbf{T}^{\mathbf{T}}$	T.T()
Diagonal	$\mathrm{diag}\,(\mathbf{T})$	diag(T)
Trace	$\mathrm{tr}\,(\mathbf{T})$	tr(T)
Deviatoric component	$\mathrm{dev}\,(\mathbf{T})$	dev(T)
Symmetric component	$\mathbf{T} = \mathbf{T}^{\mathbf{T}}$	symm(T)
Skew-symmetric component	$-\mathbf{T} = \mathbf{T}^{\mathbf{T}}$	skew(T)
Determinant	$\det(\mathbf{T})$	dev(T)
Cofactors	$\mathrm{cof}\,(\mathbf{T})$	cof(T)
Inverse	$\mathbf{T}^{-\mathbf{1}}$	inv(T)
Hodge dual	$*\mathbf{T}$	*T

When computing fluid mechanical problems, we are dealing with problems that need an approximation into discrete quantities in order to calculate a numerical solution. The approach of OpenFOAM is based on the Finite Volume Method (FVM) and therefore the problem discretisation is managed as follows [42]:

- **Spatial discretisation** The subdivision of the spatial domain into control volumes, *i.e.* the creation of computational mesh.
- **Temporal discretisation** The time domain is broken into a finite number of intervals, *i.e.* time steps Δt.
- **Equation discretisation** The PDEs are converted into a system of algebraic equations that are defined on the discretised space domain.

In this work, the discretization of Partial Differential Equations (PDE) requires a somewhat more detailed description as the concept is closely involved in the transition model implementation. The converted algebraic equations mentioned above are presented in matrix form and each term of PDE is expressed one by one in the code. OpenFOAM contains two tensor-derivative classes for expressing the differential operators with static functions. The implicit derivatives are treated with functions from *finiteVolumeMethod* class and the explicit derivatives with the *finiteVolumeCalculus* class, abbreviated by a *typedef* to *fvm* and *fvc*, respectively. It should be noted that the implicit operations return matrix coefficients whereas the explicit operations return volume fields. Table 4.3 presents the OpenFOAM derivative functions required in the transition model implementation:

Table 4.3: Derivative functions in OpenFOAM [42].

Term	Implicit/ Explicit	Mathematical expression	fvm::/fvc:: functions
Time derivative	Imp/Exp	$\partial/\partial t$ $\partial\rho\phi/\partial t$	ddt(phi) ddt(rho,phi)
Gradient	Exp	$\nabla\chi$	grad(chi)
Divergence	Exp	$\nabla\cdot\chi$	div(chi)
Laplacian	Imp/Exp	$\nabla^2\phi$ $\nabla\cdot\Gamma\nabla\phi$	laplacian(phi) laplacian(Gamma, phi)
Convection	Imp/Exp	$\nabla\cdot(\psi)$	div(psi, scheme)

The following equation (4.36) illustrates a generic transport equation that is widely utilized within the turbulence modelling:

$$\frac{\partial\rho U}{\partial t}+\nabla\cdot\phi U-\nabla\cdot\mu\nabla U=-\nabla p \tag{4.36}$$

As an example, the equation (4.36) is discretized in order to demonstrate the use of OpenFOAMs syntax in practice:

```
tmp<fvScalarMatrix> exampleEqn
(
    fvm::ddt(rho, U)
  + fvm::div(phi, U)
  - fvm::laplacian(mu, U)
  ==
  - fvc::grad(p)
);
```

4.3.2 Transition model implementation

This subsection provides a detailed "step-by-step" tutorial for the transition model implementation to OpenFoam-4.1 in Linux environment in order to provide guideline that may also be utilized in other OpenFOAM-4.x implementations. It should be noted that the users with OpenFOAM versions prior to 4.x should follow and adapt a syntax provided by other sources, for instance reference [60].

In 28th June 2016, the OpenFOAM [12] released a software version 4.0 that includes a number of changes and improvements compared to prior versions 2.x and 3.x. These new improvements affect general usability, post-processing, case management and software management. One of the major changes in the version 4.x, in contrast to the prior versions, is the alteration in the code architecture as larger

part of the source code is programmed with a template meta-programming (TMP) technique. This technique was introduced in order to allow better maintainability for the code and to accomplish more generic code structure. However, from a users point of view, the template meta-programming tends to alter the code less accessible due to its more abstract structure. Because of this modification, the implementation of turbulence models is significantly changed and the prior guidelines cannot be directly applied.

Preliminary measures

Since the code architecture is templated, it is not enough to copy only the *kOmegaSST* directory. Instead, the implementation into a templated structure requires modifications in a number of different files. Thus, the simplest approach is to copy the entire *TurbulenceModels* directory to the user directory. The following guideline is adapted from the reference [61].

```
$ OF4x
$ foam
$ cp -r --parents src/TurbulenceModels $WM_PROJECT_USER_DIR
$ cd $WM_PROJECT_USER_DIR/src/TurbulenceModels
```

Next the location of the compiled files needs to be changed in all the *Make/files*. The *Make* directories can first be found with command:

```
$ find . -name Make
```

which should give us the following directories:

```
$ ./incompressible/Make
$ ./compressible/Make
$ ./turbulenceModels/Make
```

This implies that the compiling of a single turbulence model is performed by the template code itself unlike in prior versions, where turbulence models need their own *Make* files and are compiled separately. Change the *Make/files* location in the following manner:

```
$ sed -i s/FOAM_LIBBIN/FOAM_USER_LIBBIN/g ./*/Make/files
```

Compile and check that the environment variable LD_LIBRARY_PATH points at the users working directory:

```
$ ./Allwmake
$ ldd `which simpleFoam`
  libturbulenceModels.so => /home/user/OpenFOAM/user-4.x/platforms/
  linux64GccDPInt32Opt/lib/libturbulenceModels.so
  etc...
```

The gamma transition model is implemented into the underlaying SST $k-\omega$ turbulence model that is referred to as *kOmegaSST* by OpenFOAM. Hence, it is easiest to copy the original model to a new directory and rename it to *SSTgamma*. In addition, we need to change all the references to *kOmegaSST* model in .C and .H files to point to *SSTgamma* model.

```
$ cp -r turbulenceModels/RAS/kOmegaSST turbulenceModels/RAS/SSTgamma
$ mv turbulenceModels/RAS/SSTgamma/kOmegaSST.H
  turbulenceModels/RAS/SSTgamma/SSTgamma.H
$ mv turbulenceModels/RAS/SSTgamma/kOmegaSST.C
  turbulenceModels/RAS/SSTgamma/SSTgamma.C
$ sed -i s/kOmegaSST/SSTgamma/g turbulenceModels/RAS/
  SSTgamma/SSTgamma.*
```

In the new template structure the *kOmegaSST* inherits from the class *kOmegaSST-Base*. This base class contains the functional code that needs to be altered in order to implement the code for the transitional model. We repeat the same procedures to these base files as executed above:

```
$ cp -r turbulenceModels/Base/kOmegaSST turbulenceModels/Base/
  SSTgamma
$ mv turbulenceModels/Base/SSTgamma/kOmegaSSTBase.H
  turbulenceModels/Base/SSTgamma/SSTgammaBase.H
$ mv turbulenceModels/Base/SSTgamma/kOmegaSSTBase.C
  turbulenceModels/Base/SSTgamma/SSTgammaBase.C
$ sed -i s/kOmegaSSTBase/SSTgammaBase/g
  turbulenceModels/Base/SSTgamma/SSTgammaBase.*
```

The next step is to ensure that the *SSTgamma* turbulence model is able to compile prior to the modification of the code. As mentioned before, the templated code takes care of the compilation of individual turbulence models. Hence, we need to include our *SSTgamma* model into *incompressible/turbulentTransportModels/turbulentTransportModels.C*-file. Add the following set of code in the "*RAS Models*" section:

```
#include "SSTgamma.H"
makeRASModel(SSTgamma);
```

The linking needs to be updated as well or we get an error message that the file "*SSTgamma.H*" cannot be found.

```
$ wmakeLnInclude -u turbulenceModels
```

Now compile with:

```
$ ./Allwmake
```

At this point it is worthwhile to test that a tutorial case runs with *SSTgamma* turbulence model. First we need to inform OpenFOAM to use our library by adding a following line to system/controlDict:

```
libs ("libincompressibleTurbulenceModels.so");
```

To switch on the *SSTgamma* model, we also need to change RASModel *SSTkOmega* to *SSTgamma* in *constant/turbulenceProperties*. Run the case with *simpleFoam* and check from the log that *SSTgamma* model is used.

SSTgammaBase.H modifications

First we need to declare a dimensioned scalar value named ***veldim***. This additional term is required in order to retain correct dimensions in one of the model subfunctions. In the protected data members, add following line after *dimensionedScalar c1_*;

```
dimensionedScalar minvel;
```

The transitional model requires a wall normal vector in order to calculate local argument for the pressure gradient parameter $\lambda_{\theta L}$ (equation (4.18)). Declare the wall normal vector field in *SSTgammaBase.H* after *const volScalarField& y_*:

```
const volVectorField& n_;
```

Add the declaration of intermittency variable after *volScalarField omega*:

```
volScalarField im_;
```

In the member functions section include following lines for the model to calculate effective diffusivity for intermittency:

```
//- Return the effective diffusivity for intermittency
tmp<volScalarField> DimEff() const
{
return tmp<volScalarField>
  (
       new volScalarField("DimEff", this->nut_ + this->nu())
  );
}
```

This is all the modifications required in the *SSTgammaBase.H* header file.

SSTgammaBase.C modifications

Most of the implementation code is written in *SSTgammaBase.C* file, where we define the required variables and solve the transport equation for intermittency. First modify the *kOmegaSST* blending function *F1* that is located in the private member functions section:

```
volScalarField R_y = y_ * sqrt(k_) / this->nu();
volScalarField F3_y = Foam::exp(-Foam::pow(R_y / 120.0, 8.0));
return max(tanh(pow4(arg1)),F3_y);
```

The following step is to define an additional variable *veldim* in the constructors section. Add the definition subsequent to *c1_*:

```
veldim
(
  dimensioned<scalar>
  (
    "veldim",
    dimensionSet(0, 2, -1, 0, 0, 0, 0),
    1.0
  )
),
```

The normal-to-wall vectorfield can be acquired using a class named *wallDist*. The constructor for this vectorfield is similar to wall distance and it takes the local mesh as parameter. Hence, write following line below $y_$ constructor:

```
n_(wallDist::New(this->mesh_).n())
```

Next we define the intermittency factor, an *IOobject*, by adding the following lines after the definition of *omega_*:

```
im_
(
  IOobject
  (
    IOobject::groupName("im", U.group()),
    this->runTime_.timeName(),
    this->mesh_,
    IOobject::MUST_READ,
    IOobject::AUTO_WRITE
  ),
  this->mesh_
)
```

Now all the necessary constructors are initialized. The next step is to define local parameters that are required by the models transition onset functions. All of these subfunctions are required to be solved before we can start to solve the intermittency transport equation. First, to streamlize the syntax used, we add a definition for ν right after *volScalarField& nut = this->nut_;*

```
volScalarField nu(this->nu());
```

Then the following definitions are added after *volScalarField G(this->GName(), nut * GbyNU);* in the Member functions sections:

```
volScalarField str(sqrt(S2));
volScalarField Rev(y_ * y_ * str / nu);
volScalarField vor(sqrt(2.0 * magSqr(skew(tgradU()))));
volScalarField F_limon(min(max(Rev / (2.2 * 1100.0) -1.0, 0.0), 3.0));
```

Next we couple the transition model to *kOmegaSST* by modifying energy equations source terms according to equation (4.28) and (4.31). The modified equation, with the additional source term P_k^{lim}, is presented underneath:

```
// Turbulent kinetic energy equation
tmp<fvScalarMatrix> kEqn
(
    fvm::ddt(alpha, rho, k_)
  + fvm::div(alphaRhoPhi, k_)
  - fvm::laplacian(alpha * rho * DkEff(F1), k_)
  ==
    min(alpha*rho*G, (c1_*betaStar_)*alpha*rho*k_*omega_)*im_
  + 5.0*max(im_-0.2, 0.0)*(1.0-im_)*F_limon*
    max(3.0*nu-nut, 0.0*veldim)*str*vor
  - fvm::SuSp(im_*(2.0 / 3.0)*alpha*rho*divU, k_)
  - fvm::Sp(max(im_, 0.1)*alpha*rho*epsilonByk(F1, F23), k_)
  + kSource()
  + fvOptions(alpha, rho, k_)
);
```

Note that the aforementioned parameter *veldim* is required here inside a max-function in order to maintain correct dimensions. The following step is the calculation of local arguments Tu and $\lambda_{\theta L}$ and their subfunctions of equations (4.16) and (4.22). Write the code after the line *correctNut(S2, F23);*

```
volScalarField dVdy(fvc::grad(U & n_) & n_);
volScalarField lambdaL(-0.00757 *(y_ * y_ / nu) * dVdy + 0.0128);
lambdaL = min(max(lambdaL, -1.0), 1.0);
volScalarField TuL(min(100.0 * sqrt(2.0 * k_ / 3.0) /
                  (omega_ * y_), 100.0));

//Model functions
volScalarField F_PG(im_);
forAll(im_, cellI)
{
if (lambdaL[cellI] >= 0)
  {
    F_PG[cellI]= min(1.0 + 14.68 * lambdaL[cellI], 1.5);
  }
else
  {
    F_PG[cellI] = min(1.0 - 7.34 * lambdaL[cellI] + 0.0 *
```

```
      min(lambdaL[cellI] + 0.0681, 0.0), 3.0);
    }
  }
  F_PG = max(F_PG, 0.0)
```

Now we are allowed to calculate the remaining subfunctions, local correlations, and production terms presented in equations (4.5) and (4.14):

```
  volScalarField Re_crit(100.0 + 1000.0 * exp(-1.0 * TuL * F_PG));
  volScalarField RT(k_ / (nu * omega_));
  volScalarField Fturb(Foam::exp(-Foam::pow(-(RT) / 2.0, 4.0)));
  volScalarField Fonset1(Rev / (2.2 * Re_crit));
  volScalarField Fonset2(min(Fonset1, 2.0));
  volScalarField Fonset3(max(1 - Foam::pow(RT / 3.5, 3.0), 0.0));
  volScalarField Fonset(max(Fonset2 - Fonset3, 0.0));

  volScalarField P1(100.0 * str * im_ * Fonset);
  volScalarField P2(0.06 * vor * im_ * Fturb );
```

Finally we can add the following lines for solving the intermittency transport equation (4.4):

```
  //Intermittency equation
  tmp<fvScalarMatrix> imEqn
  (
    fvm::ddt(alpha, rho, im_)
  + fvm::div(alphaRhoPhi, im_)
  - fvm::Sp(fvc::div(this->phi_), im_)
  - fvm::laplacian(DimEff(), im_)
      ==
    P1
  + P2
  - fvm::Sp(P1, im_)
  - fvm::Sp(50.0 * P2, im_)
  );

  imEqn.ref().relax();
  solve(imEqn);
```

SSTgammaBase.C file does not require further alterations. Check that the implemented code compiles by executing the following command in the */src/TurbulenceModels* directory:

```
  $ ./Allwmake
```

Additional measures

Although the actual implementation is completed, the transition model is not ready yet for running a test case. The model requires a field and boundary conditions for intermittency. Creating a field for intermittency is most straightforward by copying and modifying a file for turbulent kinetic energy field in the case directory. Conduct the following commands in the *0/* directory:

```
$ cp k im
$ sed -i s/k/im/g im
$ sed -i s/"0 2 -2 0 0 0 0"/"0 0 0 0 0 0 0"/g im
```

Next we need to set the correct boundary conditions for intermittency. Modify the *0/im* file to include the following boundary conditions given in table 4.4. In addition, OpenFOAM requires that we define discretizations for certain variables we implemented in the code. The discretizations can be defined by modifying the *system/fvSchemes* file. First change the *gradSchemes* default to Gauss linear so we do not have to define calculation of gradient separately for every new variable. Next add the following discretization under *divSchemes* section:

```
div(phi,im)     bounded Gauss upwind;
```

Then add discretization for the effective diffusivity of intermittency under *laplacianSchemes*:

```
laplacian(DimEff, im)    Gauss linear corrected;
```

Furthermore, we need to determine how intermittency is solved from the transport equation. To define the solver, add the following in *system/fvSolution* file under the solver section:

```
im
{
    solver          PBiCG;
    preconditioner  DILU;
    tolerance       1e-10;
    relTol          0.1;
}
```

Also define the relaxation factor for intermittency under *relaxationFactors*:

```
im      0.7;
```

All the required modifications are now completed and the transitional model is ready to be tested with a flat plate case.

Table 4.4: Boundary conditions for the intermittency.

Field	**Condition**
internalField	uniform 1
inlet	fixedValue uniform 1
outlet	zeroGradient
symmetry	symmetryPlane
flatplate	zeroGradient

Chapter 5

Transition Simulations

In this Chapter, the OpenFOAM simulations with the implemented γ-model [1] are presented. The chapter provides a numerical setup for all the test cases in conjunction with obtained results and discusses the main outcome. In the first section 5.1, the basic configuration of the simulations is described. Section 5.2 verifies the implementation as well as determines a suitable default setup for the model validation cases. In Section 5.3, the implemented model is validated for zero pressure gradient flat plate test cases. A response to freestream variables is investigated in the Section 5.4 for the original transition model as well as for a suggested variant of the model.

5.1 Default configuration

All the results shown in this Chapter have been computed applying the following configuration for the simulations. All test cases were calculated with assumptions of incompressible flow and Newtonian fluid. The SST $k-\omega$ [37] was used as the underlying Low-Re turbulence model in the simulations, excluding the cases with the suggested variant of the transition model, which was coupled with SST-sust turbulence model. Diffusion and gradient terms were treated with high-resolution second-order discretization schemes. However, an additional study for the discretization of convection terms was performed (see Appendix A), since earlier studies have shown the previous LCTM models being sensitive to the selected convection schemes [44]. According to the obtained findings, the velocity term was treated with a bounded second-order upwind biased extrapolations, whereas a TVD scheme was employed on other convection terms. All simulations were calculated using the *simpleFoam* solver, which is an OpenFOAM implementation of the SIMPLE solution algorithm for incompressible flow cases (see section 3.4). In the algorithm, the under relaxation factor of pressure term was set to value of 0.3, while the rest terms were treated with a factor set to value of 0.7. The used hardware included a Intel Xeon(R) CPU E5-1650 3.20GHz ($\times$12) processor and 15.5 GiB of memory. This setup was run on 64-bit Linux using Fedora 24 distribution without utilizing a parallel calculation.

To achieve grid independent solutions for the γ-model, meshes were constructed according to the following practice guidelines given by Menter [1]:

- At least 30 nodes across the boundary layer
- More than 100 nodes in streamwise direction
- Dimensionless wall distance should be less than one: $y^+ < 1$
- Wall normal expansion ratio should be small enough: $R < 1.1$

Although these guidelines provide efficient meshes for simple flat plate cases, it was found important to investigate a solution behaviour on alternative grids due to a peculiar behaviour that has been observed for the prior $\gamma - Re_{\theta t}$ model by Langtry [44]. Hence, an additional mesh study was carried out (see Appendix B) in order to examine the model feasibility for standard turbulence model verification grids provided by NASA [41].

The applied boundary conditions are presented in Figure 5.1, which also shows the spatial dimensions used for grids in all the test cases. The computational grids included a short inlet region of 0.1 meter to eliminate possible interference due to inlet, and they were refined within the regions of highest gradients, that are near the surface and at the beginning of the plate.

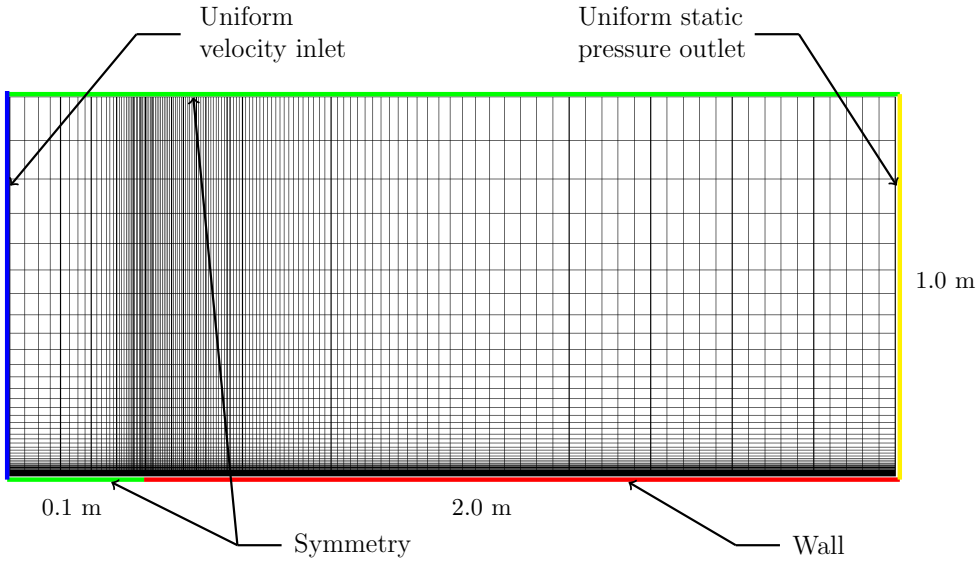

Figure 5.1: Flate plate mesh with boundary conditions.

It should be emphasized that the inlet conditions were calibrated according to the freestream turbulence decay within the inlet region (see Appendix C) for achieving correct conditions at the leading edge of the plate.

5.2 Model verification

The γ-model implementation was verified by applying first a discretization and convergence study (see Appendix A) to define proper setup for discretization schemes. This was followed by an additional mesh study on a zero pressure gradient flat plate using grids provided by NASA turbulence modelling resource (see Appendix B). This section presents the results of the T3A validation case [62] that were used to ensure a proper function of the implementation. Since the model intervenes with the boundary layer modelling, a possible error in the code might generate results dissimilar to the reported characteristics. Therefore, the properties of simulated boundary layers were analyzed and compared to theoretical as well as to the experimental values. Several variables were examined, including velocity, intermittency, turbulent kinetic energy, specific turbulence dissipation rate and freestream turbulence intensity.

5.2.1 Numerical setup

Identical computational grids were used for all the test cases, for which details are given in table 5.1. Employed boundary conditions and mesh dimensions were in accordance with those presented in Figure 5.1. The initial inlet values were adjusted in order to rule in the effects of freestream turbulence decay (see Appendix C) within the inlet region and are described in table 5.2. The applied inlet conditions for the turbulent variables were the same as the ones used by Menter for the T3A validation case [1]. It should be noted that the eddy viscosity ratio is a nonphysical quantity required for RANS modelling. The default setup for discretization schemes can be found from Appendix A.

Table 5.1: Mesh for verification cases.

Grid	Nodes	R (x, y)	First cell (x, y)	y^+
T3A mesh	$240 \times 160 \times 1$	1.05	2×10^{-5} [m]	< 0.5

Table 5.2: Inlet values for T3A test.

T3A	U [m/s]	Tu (%)	μ_t/μ
Initial	5.18	3.3	12
Adjusted	5.18	4.2	12

5.2.2 Simulation results

The skin friction coefficient provides a good indication of the transition location. This can be seen in Figure 5.2 that shows the skin friction distribution for the γ-model and the default SST $k-\omega$ turbulence model. For the transitional model, the distribution agrees well with the measured values and the theoretical curves for a laminar and a turbulent boundary layer. Hence, it can be deduced that the implementation was able to include the transitional effects into the calculations and furthermore the model itself seems to predict transition accurately in this test case. In contrast, the default turbulence model generates results corresponding to the theoretical curve of turbulent boundary layer for entire distance of the plate, however, somewhat underestimating the turbulent skin friction.

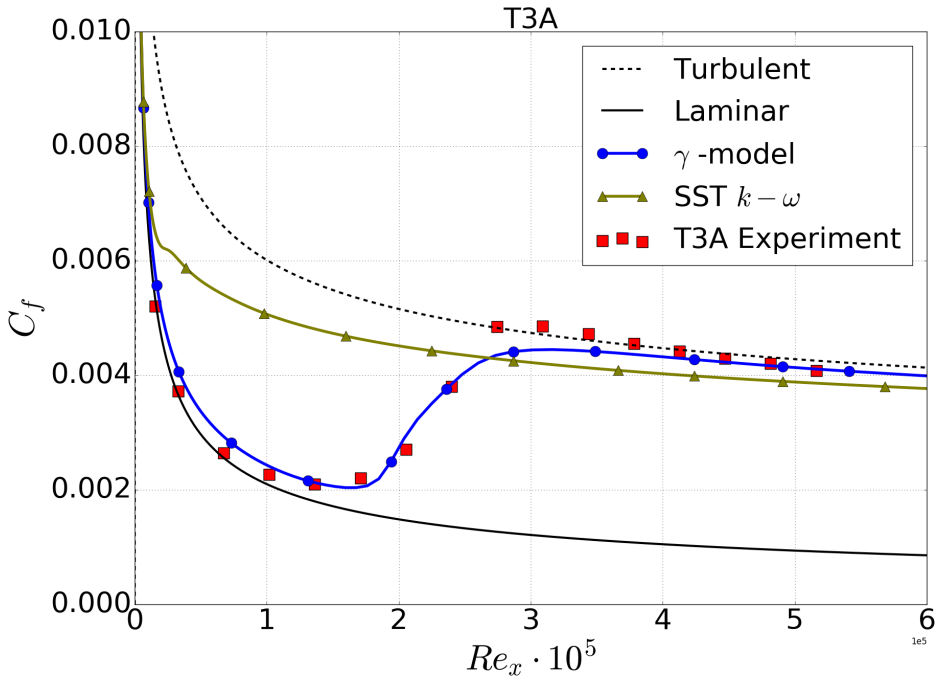

Figure 5.2: Skin friction on the flat plate.

Figure 5.3 presents the simulated decay of freestream turbulence in comparison with experimentally obtained values. The simulated pattern corresponds well with experimental values along the flat plate, which confirms that the inlet conditions were rightfully adjusted, hence should not induce errors within simulation. The freestream turbulence decay is connected to the eddy viscosity ratio which determines a value of the specific turbulence dissipation ω with inverse relation: large eddy viscosity ratios result in low decay rates of turbulence.

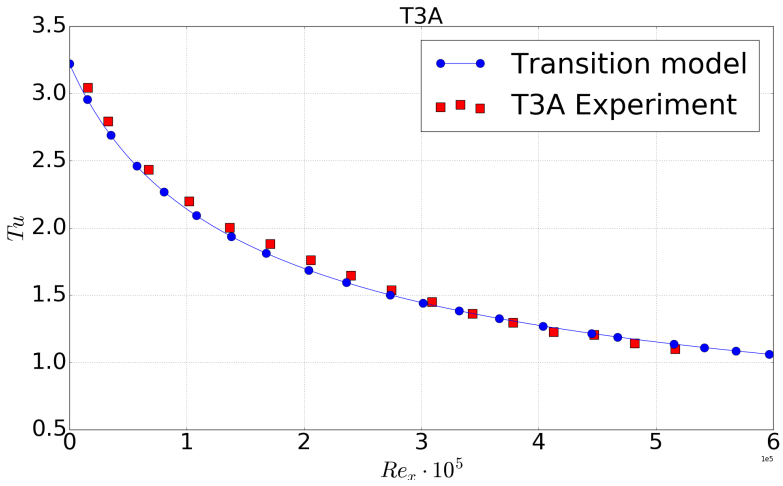

Figure 5.3: Decay of freestream turbulence intensity.

The simulated velocity profiles within the boundary layer are presented in Figure 5.4. As shown in Figure 5.4a, the produced velocity profiles agree well with theoretical shapes for both laminar ($Re_x = 100\,000$) and turbulent ($Re_x = 620\,000$) flow regions. In Figure 5.4b, the dimensionless velocity profile of the turbulent boundary layer follows closely the analytic fittings, and thereby confirms the layer is resolved with a sufficient accuracy.

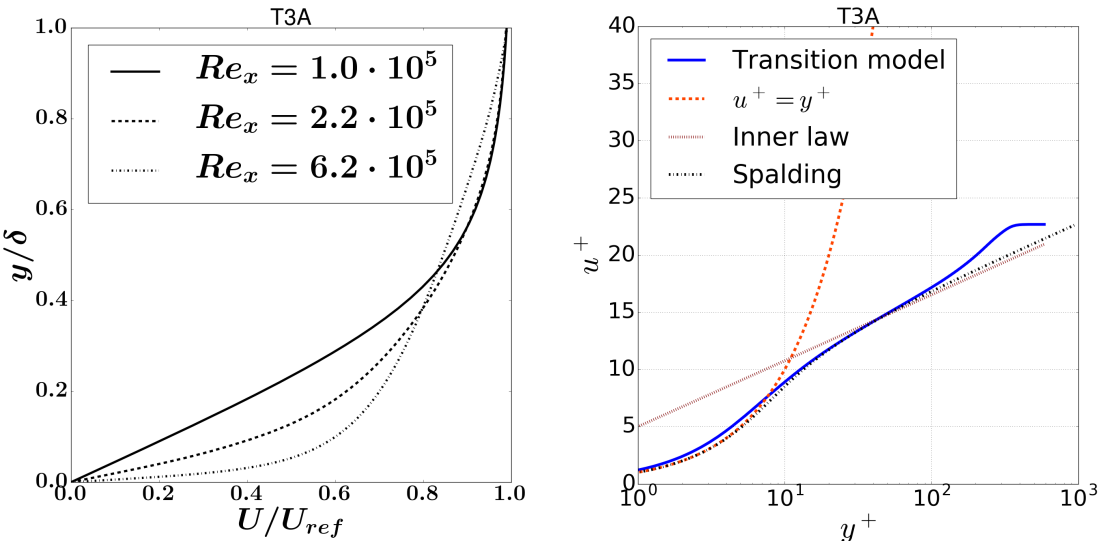

(a) (b)

Figure 5.4: (a) Flat plate velocity profiles, (b) Dimensionless profile of a turbulent boundary layer ($Re = 6.2 \cdot 10^5$).

Figure 5.5 shows the behaviour of turbulent variables within the boundary layer in three different locations, which represent the laminar ($Re_x = 1.0 \cdot 10^5$), transi-

tional ($Re_x = 2.2 \cdot 10^5$) and turbulent ($Re_x = 6.2 \cdot 10^5$) cross-sections of the boundary layer. Expected behaviour can be seen for the turbulence kinetic energy (Figure 5.5a), which clearly increases within the boundary layer as the flow transforms into turbulent. The same notion applies for the turbulence specific dissipation, which reduces inside the boundary layer on higher Reynolds numbers signifying reduced turbulence dissipation and thereby increased eddy viscosity in the turbulent cross-section. As shown in Figure 5.5c, the calculated intermittency factor remains zero near the surface in the case of laminar flow, where it is activated approximately in the midpoint of the layer. In the turbulent flow, the intermittency factor has zero values only within a thin region describing the viscous sublayer, where the turbulence is damped out by the molecular viscosity. According to these results, the turbulent variables have sensible values and are thereby correctly modelled within the boundary layer.

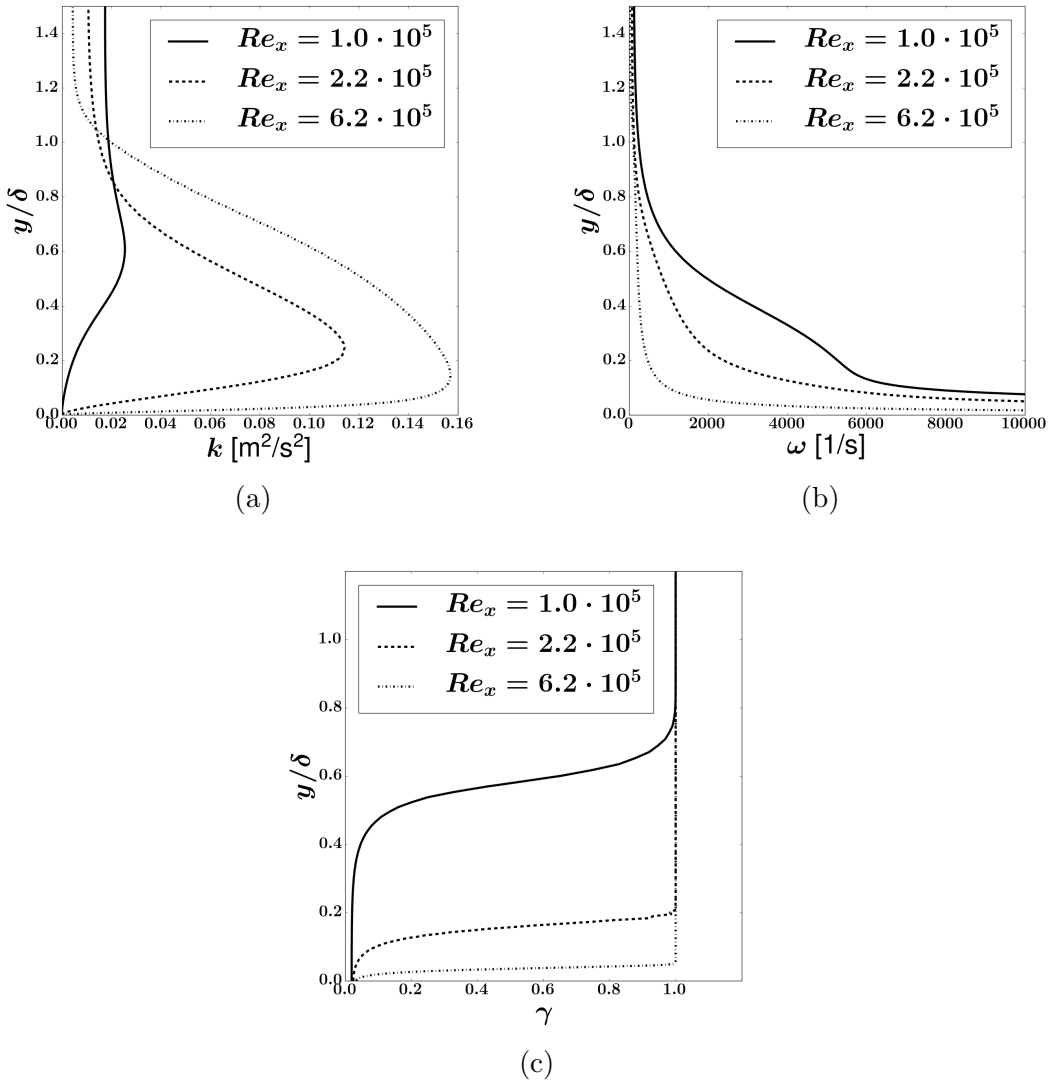

(a) (b)

(c)

Figure 5.5: Turbulent variables within the boundary layer.

5.3 Model validation for flat plate test cases

A skin friction distribution serves as a good indicator of transition and offers means for validating the implemented transition model. Hence, the γ-model was applied on four zero pressure gradient test cases: three T3 test cases of the ERCOFTAC flat plate experiments [62] and the Schubauer-Klebanoff experiment [63]. The T3 transition experiment series were performed by Rolls Royce in the early 1990's and have become a somewhat standard for transition model validation cases. All the T3 cases have high freestream turbulence intensities, hence the by-pass mode dominates the transition. The Schubauer-Klebanoff experiment [63] was originally conducted in 1950's and represents a natural transition with low freestream turbulence intensity values on a flat plate.

Table 5.3 describes the inlet conditions at the leading edge of the flat plate for validation cases. These are identical to the ones used in the original model validation by Menter [1]. The decay of freestream turbulence within the inlet region was taken into account (see Appendix C), and all calculations were carried out for each test until convergence.

Table 5.3: Inlet values for flat plate tests [1].

Test case	U [m/s]	Tu (%)	μ_t/μ
T3A	5.18	3.3	12
T3B	9.4	6.2	90
T3A-	19.8	0.9	8
Schubauer-Klebanoff	50.1	0.03	1

5.3.1 Numerical setup

All meshes used in the validation cases had same dimensions and complied with the criteria presented above. The T3 cases were simulated using the same grid whereas the Schubauer-Klebanoff test case required a somewhat finer mesh for maintaining y^+ below values of one. A detailed description for these two grids are presented in table 5.4.

Table 5.4: Mesh details for validation cases.

Grid	Nodes	R (x, y)	First cell (x, y)	y^+
T3-cases	$240 \times 160 \times 1$	1.05	2×10^{-5} m	< 0.5
S&K	$280 \times 169 \times 1$	1.05	1×10^{-5} m	≈ 0.5

The Tu decay within the mesh inlet region was taken into consideration by employing equation (C1) given in Appendix C for calculating the adjusted value at the inlet. Table 5.5 presents the adjusted inlet values for each test case.

Table 5.5: Applied inlet values for flat plate tests.

Test case	Tu (%)	k	ω	μ_t/μ
T3A	4.2	0.071	394.4	12
T3B	7.2	0.766	567.1	90
T3A-	1.0	0.059	490.1	8
Schubauer-Klebanoff	0.1	0.0003	22.59	1

5.3.2 Simulation results

Figure 5.6 shows the simulated skin friction distributions for the zero pressure gradient cases in comparison with the experimental results. The results using the previous $\gamma - Re_{\theta t}$ model are displayed for comparison. In addition, the figure illustrates the theoretical skin frictions for a laminar and a fully turbulent boundary layer given by equations (2.17) and (2.23), respectively.

In general, the predicted skin friction distribution using γ-model is in good agreement with the experimental values and follows the theoretical skin friction curves outside the transition region. For three test cases (T3A, T3B, Schubauer-Klebanoff), the model is able to predict the transition location with an excellent accuracy. In T3A case (figure 5.6a), the modelled skin friction is consistent with the experimental results, however, remains on somewhat lower levels at the beginning of the turbulent boundary layer. In T3B case (figure 5.6b) that has the highest freestream turbulence intensity (6.2%), the model resuls in smoother curves in the transition region. The natural transition of the Schubauer-Klebanoff experiment (figure 5.6d) is also predicted with a good accuracy. However, in the T3A- case (figure 5.6c), the model failed to predict the correct transition location by on-setting the turbulence prematurely ($Re_c = 1.4 \times 10^6$). Although the difference to experimental results ($Re_c = 1.75 \times 10^6$) is rather large, this outcome conforms with that documented for the same test case in the original publication by Menter [1].

In contrast to the prior LCTM model, the γ-model predicts transition location with a better accuracy in all the test cases. However, it should be noted that the $\gamma - Re_{\theta t}$ model underachieved in each test case compared to results by Menter [1]. This is most likely due to the Langtry-Menter transition model desideratum for specific inlet conditions, which in these cases were identical for both models. Moreover, the $\gamma - Re_{\theta t}$ OpenFOAM implementation is not yet validated, thereby being also a possible source for discrepancies within the calculations.

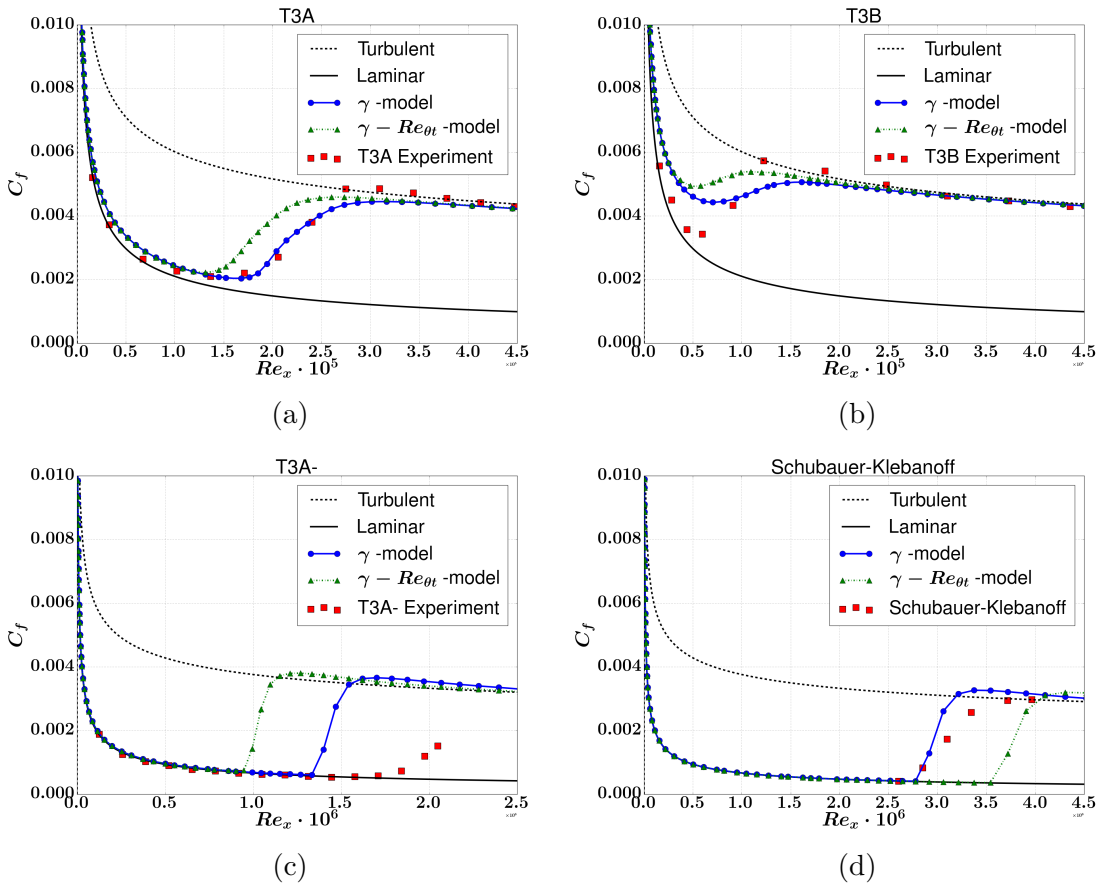

Figure 5.6: Skin friction distribution on a flat plate.

Figure 5.7 shows the decay of freestream turbulence intensity for the T3 test series (for Schubauer-Klebanoff test no such data was available). It is seen that the simulated freestream turbulence intensity matches well the experimentally obtained values in all three test cases. These results indicate that the discrepancy in the T3A-case transition location prediction (figure 5.6c) is most likely caused by some other factors than by thefreestream turbulent variables.

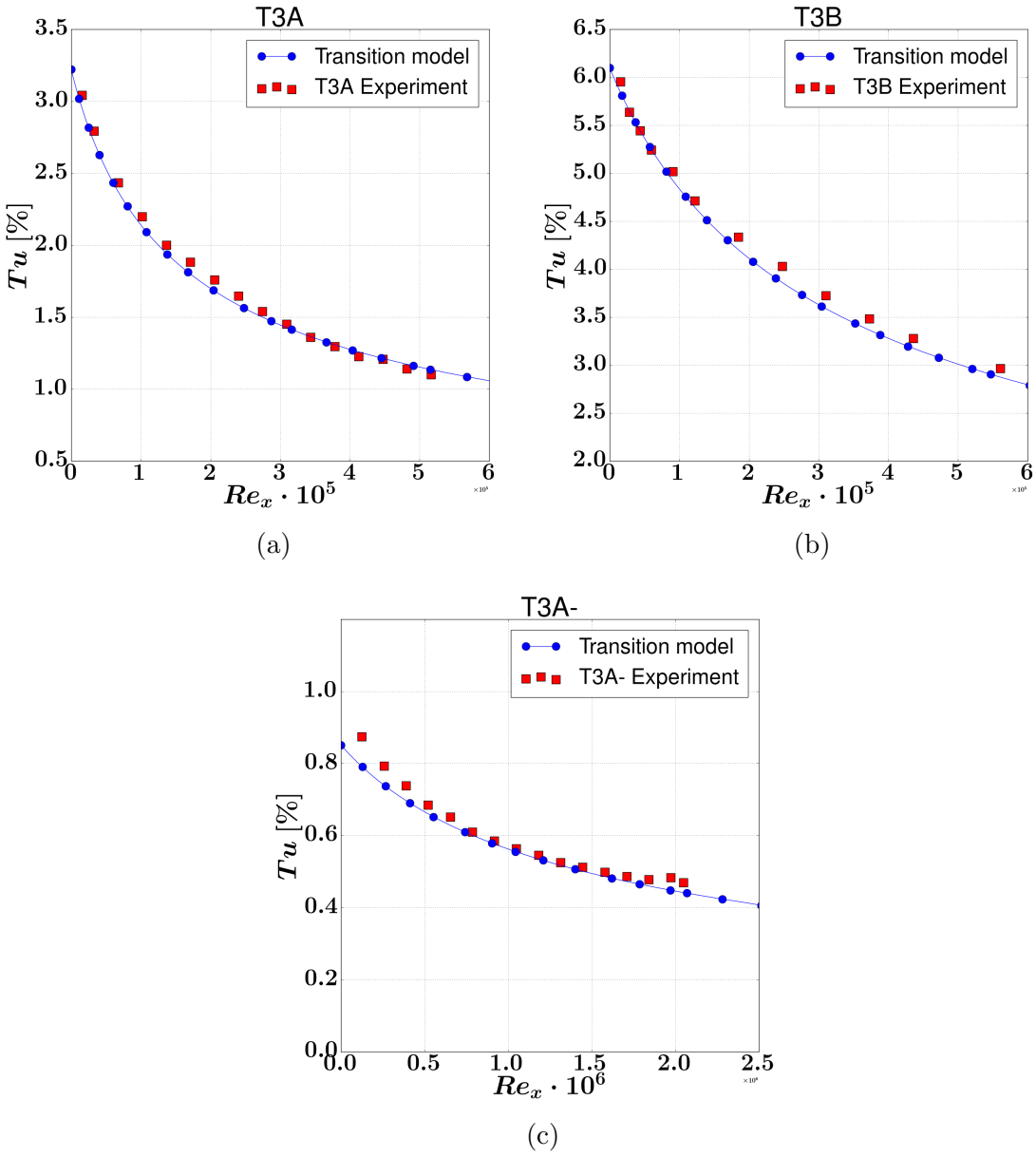

Figure 5.7: Decay of the freestream turbulence intensity as a function of a streamwise distance.

The solution convergence history for the validation cases can be seen in Figure 5.8, which presents the residual development with respect to the iteration rounds. All simulations converge smoothly without oscillations and residuals diminish to low values. The convergence seems to be much slower in the T3B (Figure 5.8b) and Schubauer-Klebanoff (Figure 5.8d) cases where the solution stops changing after about 12 000 iterations.

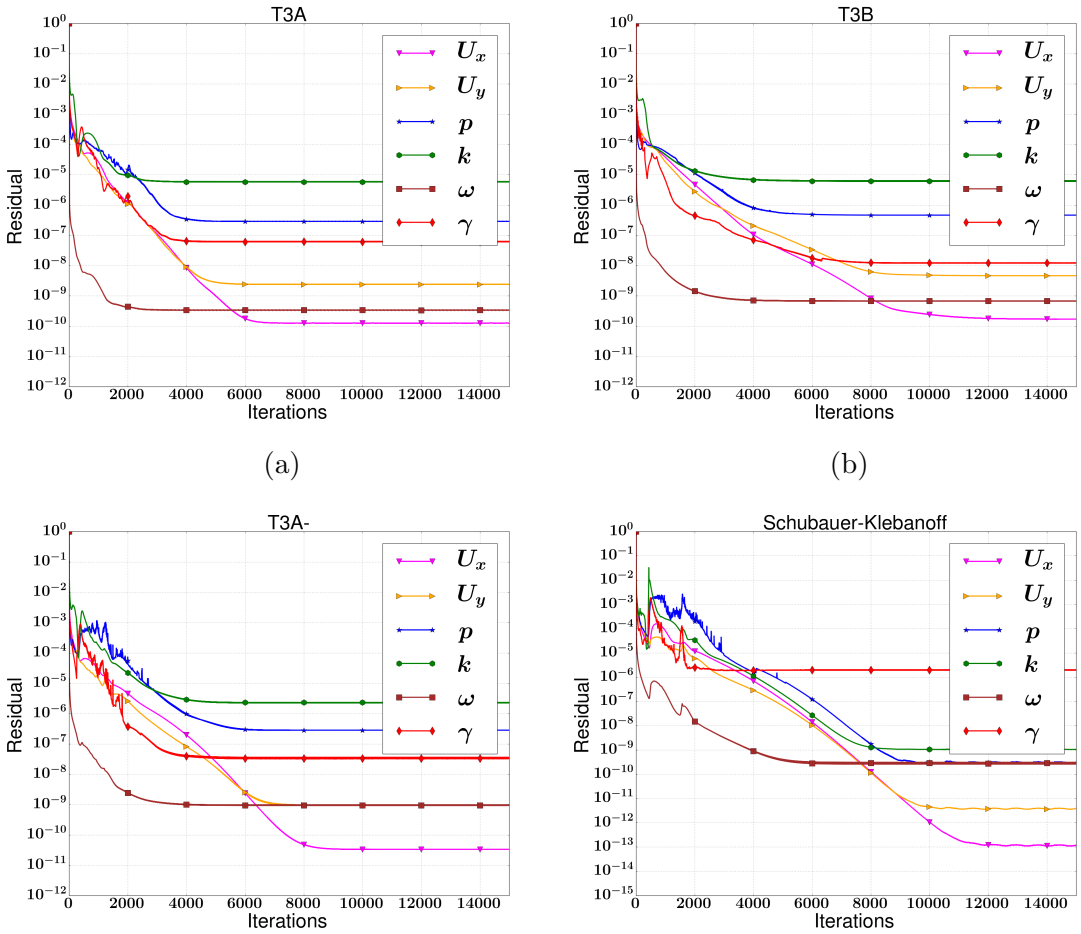

Figure 5.8: Convergence history of the validation cases.

Table 5.6 describes the CPU times required for achieving a converge in four test cases using three different models. It should be noted that these are rather coarse approximations since the minimum limit of residuals was set significantly low (10^{-20}) resulting in dissimilar level of accuracy in state of converge between the models. However, the results indicate that γ-model requires only approximately ten percent of additional computational time in comparison with the default SST $k-\omega$ turbulence model. The $\gamma - Re_{\theta t}$ model is notably more resource-intensive by requiring additional fourty-six percent of CPU time. This is approximately double to that previously observed for the $\gamma - Re_{\theta t}$ model by Nikulainen [64]. The reason for this large discrepancy remains unclear, however, it is most likely connected to dissimilarities in the model implementation. Nevertheless, as expected, the γ-model seems to be more efficient than the previous two-equation model.

Table 5.6: CPU times [s] for models in flat plate cases.

	SST $k-\omega$	γ-model	$\gamma - Re_{\theta t}$	γ-sust
T3A	2373	2738	4941	4900
T3B	6560	5846	6933	6845
T3A-	4779	5103	8050	5130
S&K	4866	6674	7217	4830
Total time	18578	20361(+9.6%)	27141(+46.1%)	21705(+16.8%)

5.4 Response to freestream turbulence variables

The SST $k-\omega$ turbulence model produces unrealistically rapid decay of freestream turbulence [14], which has to be considered when determining inlet conditions for transition simulation in case of external flows. This decay is dependent on the inlet eddy viscosity ratio (μ_t/μ) whose determination itself is a source of uncertainties within turbulence modelling. Although this behaviour can be taken into account by applying equation (C1) given in Appendix C, it restricts the mesh inlet region to relatively short dimensions, thereby having a possible influence on the solution. Moreover, it has been observed by several studies that LCTM models show significant sensitivity to freestream turbulence levels [15, 64]. This in conjuction with the turbulence decay makes the transition prediction very dependent of the chosen combination for the inlet values.

Therefore, the γ-model was tested against a wide range of inlet conditions for the freestream turbulence intensity as well as for the eddy viscosity ratios in order to investigate the model sensitivity to these factors. Furthermore, these tests were repeated using a variant of the γ-model that was implemented into the SST-sust turbulence model [14], which contains a controlled decay of turbulence variables. This variant is referred to as the γ-sust model in this paper from now on. Not only does this approach of applying sustained turbulence function in good reference to the original model, it removes the transition model dependency on the turbulence decay, and thereby eliminates the reliance on the inlet region dimensions of the mesh.

First, the models were tested against a range of eddy viscosity ratios by altering the eddy viscosity at inlet while keeping the freestream turbulence intensity constant. The next set of simulations included similar tests, however, this time the eddy viscosity ratio was fixed while altering the inlet conditions for freestream turbulence intensity. All simulations were performed on the T3A case, which also served as the default case in the model verification.

5.4.1 Numerical setup

The simulations for varying freestream turbulence variables were performed using the same default setup as in T3A validation case, including computational mesh,

boundary conditions, discretization and solvers. The freestream turbulence intensity was calibrated according to turbulence decay for each test case simulated with the initial transition mode. This is required as the specific turbulence dissipation rate ω of the underlaying turbulence model is influenced by the eddy viscosity ratio μ_t/μ. It should be also noted that cases run with the γ-sust model did not need such calibration due to the inherent absence of turbulence decay.

Two sets of simulations with varied eddy viscosity ratios were performed for which the inlet conditions are described in table 5.7. The response to freestream turbulence intensity was examined by varying the inlet values between 0.5 percent to 5.0 percent ($Tu = 0.5 - 5.0\%$) using a half percent interval, resulting in total of ten simulations per model. It should be noted that a larger eddy viscosity ratio ($\mu_t/\mu = 20$) was used for the γ-sust model in the Tu tests due to observations based on the previous eddy viscosity ratio simulations.

Table 5.7: Inlet conditions for the eddy viscosity ratio.

T3A	μ_t/μ					
Set 1	0.1	1	10	50	100	200
Set 2	3	6	9	12	15	18

5.4.2 Simulation results

Figure 5.9 shows the modelled skin frictions for the T3A test case against a wide range of eddy viscosity ratios. Generally, the eddy viscosity ratio seems to have a similar influence on both models. Low eddy turbulent viscosity levels ($\mu_t/\mu \leq 1$) result in a laminar boundary layer, as the turbulence production is not triggered during the distance of the plate. With high ratios ($\mu_t/\mu \geq 50$), the transition onset is shifted towards the leading edge compared to the experimental results. However, increasing the eddy viscosity above this level does not seem to affect the predicted onset of transition, which remains stationary and is near identical for both models. A notable feature is that both models seem to be remarkably sensitive to intermediate eddy viscosity ratios ($1 < \mu_t/\mu < 50$). Especially the γ-sust model shows unexpected behaviour by predicting a steeper transition in a slightly earlier location with significantly deviating skin friction distribution. Hence, additional tests were performed focusing on the aforementioned interval.

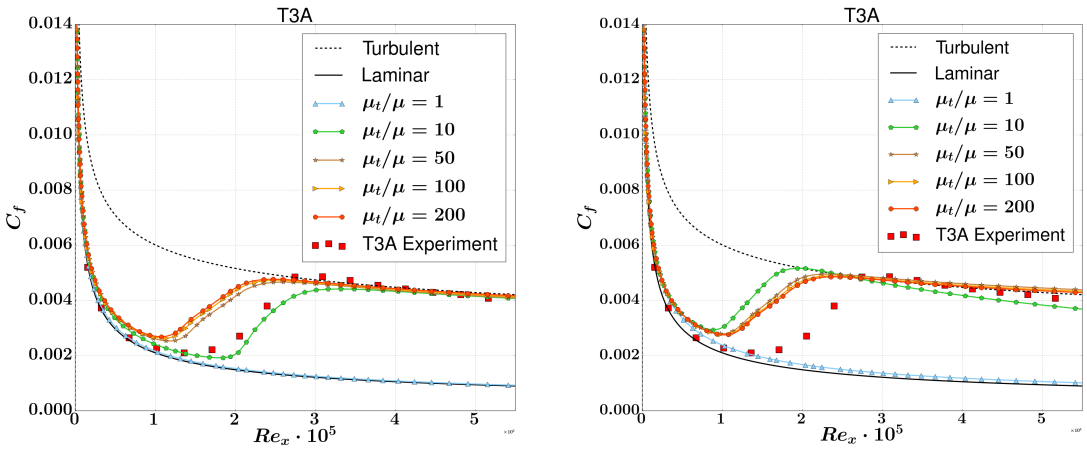

(a) γ-model (b) γ-sust model

Figure 5.9: T3A test case with varied eddy viscosity ratios.

Figure 5.10 shows the simulated skin friction distribution against intermediate eddy viscosity ratios. The results differ drastically between the tested models, for which completely divergent behavior can be seen. In case of the γ model, an increment in the viscosity ratio shifts the transition location towards the leading edge, as can be seen in Figure 5.10a. The transition onset appears to be most impacted by low eddy viscosity ratios ($\mu_t/\mu \leq 9$), and with sufficiently low ratios ($\mu_t/\mu = 3$) the flow remains entirely laminar. This is most likely connected to the freestream turbulence decay rate that is inversely proportional to the eddy viscosity ratio (see Appendix C). Although the transition location is clearly influenced, the model succeeds to produce the theoretical values for the skin friction outside the transition region. These results indicate that using intermediate eddy viscosity ratios ($1 \leq \mu_t/\mu \leq 15$) in a case of relatively high Tu value ($Tu = 3.3\%$) results in an unreliable transition onset prediction.

Figure 5.10b illustrates that the transition model using controlled decay yields in completely different behaviour. Surprisingly, the variation of the viscosity ratio had no effect on the predicted transition location excluding the simulation with the lowest value ($\mu_t/\mu = 3$), which resulted the transition point to shift slightly downstream. Instead, the results show deviation from the theoretical turbulent skin friction with a similar logarithmic relation than observed for the transition location using the original implementation. With the highest viscosity ratio ($\mu_t/\mu = 18$), the modelled skin friction distribution is approximately in accordance with the theoretical curve. Results indicate that the γ-sust model achieves a more robust prediction for transition locations than the γ-model in cases of intermediate eddy viscosity ratios. However, with identical inlet conditions the transition onset is premature, and a higher eddy viscosity ratio is required to obtain correct skin friction distribution for a turbulent boundary layer.

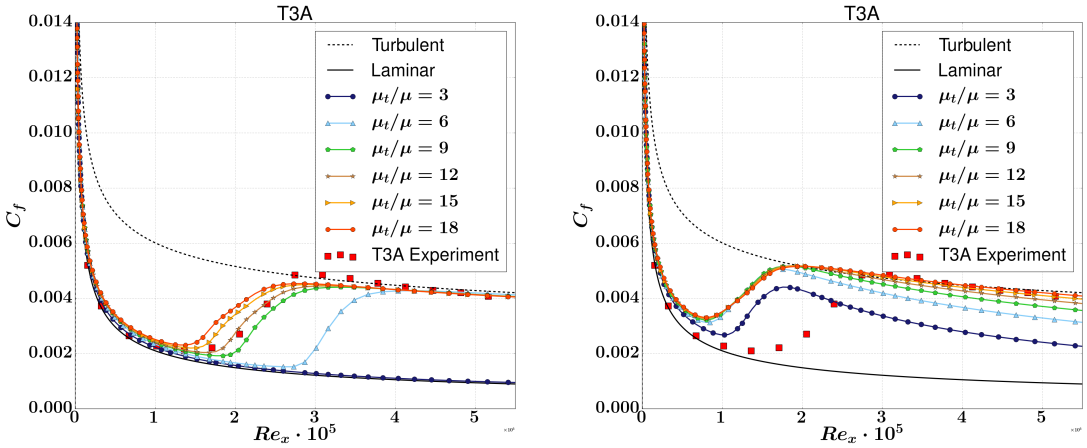

(a) γ-model (b) γ-sust model

Figure 5.10: T3A test case with intermediate eddy viscosity ratios.

The correspondence to the varied levels of the freestream turbulence intensity is shown in Figure 5.11. It can be seen that an increment in the freestream turbulence intensity shifts the transition location towards the leading edge. This is an expected result since Tu represents the disturbance in the freestream. Hence, the higher levels of Tu lead naturally to an earlier occurrence of the transition location. However, a distinguishable feature between the models can be observed. The γ-sust model reacts more sensitively to high Tu levels $(3.5 - 5.0\%)$ compared to the γ-model.

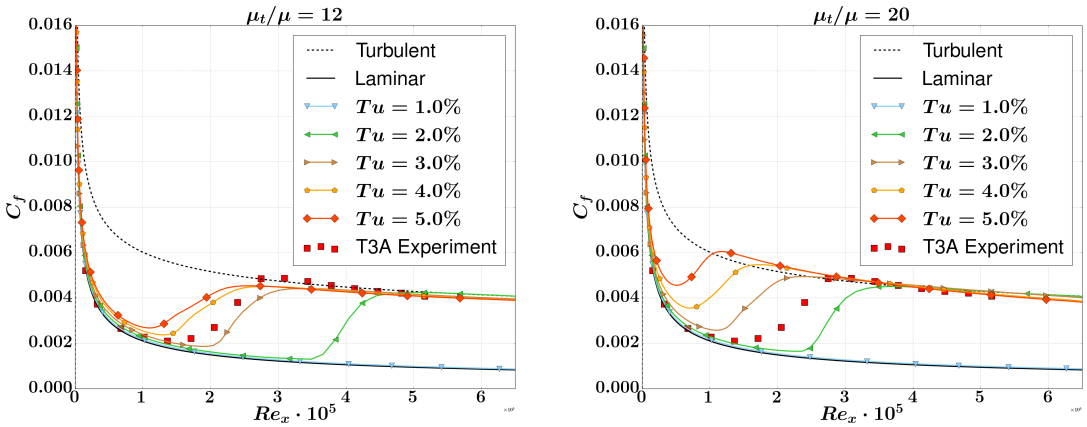

(a) γ-model (b) γ-sust model

Figure 5.11: Response to the freestream turbulence intensity.

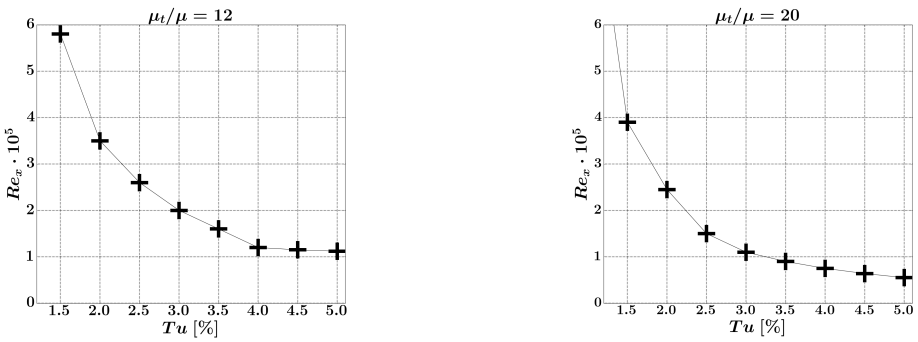

(a) γ-model (b) γ-sust model

Figure 5.12: Transition location as a function of the freestream turbulence intensity.

Figure 5.13 shows the predicted skin friction distributions for the zero pressure gradient validation cases using the γ-sust model. It can be seen that the transition onset is prematurely predicted in the T3A (Figure 5.13a) and T3A- (Figure 5.13c) cases. The turbulent skin friction coefficients also obtain slightly wrong levels due to the eddy viscosity ratio. However, the overall results are very promising and surprisingly close to the results of the original γ-model, considering no additional calibration was performed for the coupling with the SST-sust turbulence model.

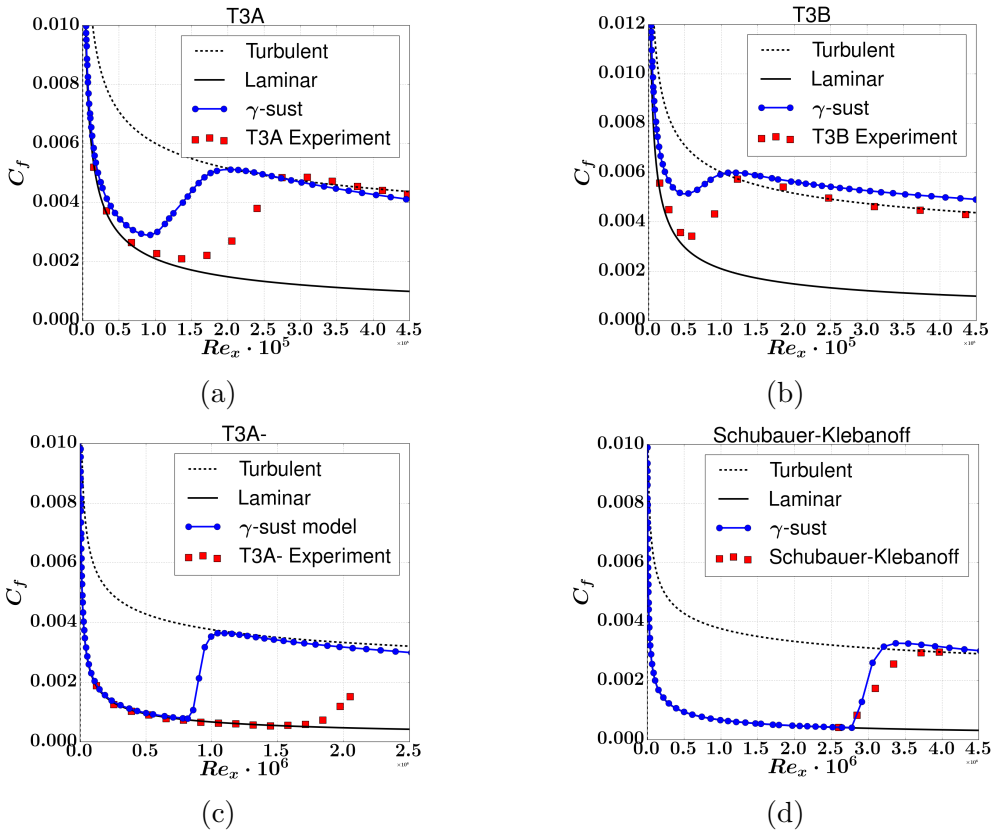

(a) (b)

(c) (d)

Figure 5.13: Skin friction distribution on a flat plate with γ-sust model.

Chapter 6

Summary and Conclusions

In this thesis, the One-equation Local Correlation-based Transition Model by Menter et al. [1] was implemented into the OpenFOAM CFD software and validated for flat plate cases with a zero pressure gradient. The implementation was achieved by modifying OpenFOAM's C++ source code, in which the transition model was coupled with the SST $k-\omega$ turbulence model [40]. A detailed tutorial on implementation of the γ-model was constructed that is compatible for OpenFOAM 4.x versions in the Linux-environment. In addition, the model's performance against varied freestream turbulence variables was reviewed, and compared to a suggested variant of the model coupled with the SST-sust turbulence model that uses a controlled decay of turbulence [14].

In general, the γ-model performed well and was able to include the effects of the by-pass transition and the natural transition, which were the dominating transition modes in the simulations. In the zero pressure gradient validation cases, the predicted locations for transition onset and the skin friction distributions were in good agreement with the experimental results documented by Rolls-Royce [65], and by Schubauer and Klebanoff [63]. Although the transition model was able to generate fair results under specific conditions, it was observed that the simulation results were dependent on multiple individual factors, such as grid quality, discretization and freestream turbulence variables. This makes the preparation for simulations more difficult, and thereby complicates the applicability of the transition model to general flow cases. Especially the dependency of the results on the decay of freestream turbulence brings with it additional uncertainties, as it is not only connected to the eddy viscosity ratio, but also to the dimensions of the computational grid.

The further studies with varied inlet conditions for turbulence variables showed that a predicted transition location was heavily dependent on intermediate eddy viscosity ratios, in addition to the freestream turbulence intensity, a variable to which the prior LCTM model had already been shown to have a high sensitivity. This is a problematic feature for many practical flow cases of high turbulence intensity, such as in turbo-machinery flows, where the combination of freestream turbulence variables plays an important role. Nevertheless, the simulations using the suggested variant were promising and indicated the γ-model to be compatible with the SST-sust tur-

bulence model. Although the γ-sust model was unable to achieve the accuracy of the original implementation, the simulations showed that the predicted transition location was significantly less affected by the eddy viscosity ratio. Hence, it seems that with appropriate calibration this approach has the potential to produce more robust results in complex flow conditions than the default model coupled with the SST $k-\omega$ turbulence model.

Hence, the most intriguing topic in future would be a further investigation and calibration of the γ-model coupled with the SST-sust turbulence model, since this approach would eliminate the unwanted decay of turbulence variables and therefore also remove the dependency on the inlet dimensions of the computational grids. For this purpose, it would be necessary to first perform feasibility studies for the approach in more generic flow cases by examining the γ-sust model behaviour under varying pressure gradients in two and three-dimensional cases. A natural follow-up for this work would include validating the implementation to cover adverse and favourable pressure gradients in flat plate cases, followed by a validation for two-dimensional and three-dimensional cases. Another topic for future work would be to extend the γ-model to to account for additional effects, such as surface roughness and cross-flow transition, which would be a significant improvement towards better overall transition modelling. The initial approach for this might be to study the feasibility of using the previously developed extensions for the $\gamma - Re_{\theta t}$-model (*e.g.* surface roughness by Lange et al. [9] and crossflow by Müller et al. [10]), which have already been implemented into OpenFOAM as well as validated in the thesis by Kruljevic [15].

Bibliography

[1] F. R. Menter, P. E. Smirnov, T. Liu, and R. Avancha, "A one-equation local correlation-based transition model," *Flow, Turbulence and Combustion*, vol. 95, no. 4, pp. 583–619, 2015.

[2] F. R. Menter, R. Langtry, S. Likki, Y. Suzen, P. Huang, and S. Völker, "A correlation-based transition model using local variablesâpart i: model formulation," *Journal of turbomachinery*, vol. 128, no. 3, pp. 413–422, 2006.

[3] D. K. Walters and D. Cokljat, "A three-equation eddy-viscosity model for reynolds-averaged navier–stokes simulations of transitional flow," *Journal of fluids engineering*, vol. 130, no. 12, p. 121401, 2008.

[4] S. Kubacki and E. Dick, "An algebraic model for bypass transition in turbomachinery boundary layer flows," *International Journal of Heat and Fluid Flow*, vol. 58, pp. 68–83, 2016.

[5] X. Ge, S. Arolla, and P. Durbin, "A bypass transition model based on the intermittency function," *Flow, turbulence and combustion*, vol. 93, no. 1, pp. 37–61, 2014.

[6] R. Pacciani, M. Marconcini, A. Arnone, and F. Bertini, "Predicting high-lift low-pressure turbine cascades flow using transition-sensitive turbulence closures," *Journal of Turbomachinery*, vol. 136, no. 5, p. 051007, 2014.

[7] R. B. Langtry and F. R. Menter, "Correlation-based transition modeling for unstructured parallelized computational fluid dynamics codes," *AIAA journal*, vol. 47, no. 12, pp. 2894–2906, 2009.

[8] E. Dick and S. Kubacki, "Transition models for turbomachinery boundary layer flows: a review," *International Journal of Turbomachinery, Propulsion and Power*, vol. 2, no. 2, p. 4, 2017.

[9] C. M. Langel, R. Chow, C. van Dam, M. A. Rumsey, D. C. Maniaci, R. S. Ehrmann, and E. B. White, "A computational approach to simulating the effects of realistic surface roughness on boundary layer transition," in *52nd Aero. Sci. Meeting, Chicago, USA*, pp. 1–16, 2014.

[10] C. Müller and F. Herbst, "Modelling of crossflow-induced transition based on local variables," *Proc. ECCOMAS, Paper*, no. 2252, 2014.

[11] R. B. Langtry, K. Sengupta, D. T. Yeh, and A. J. Dorgan, "Extending the $\gamma - \mathrm{Re}_{\theta t}$ local correlation based transition model for crossflow effects," in *45th AIAA Fluid Dynamics Conference*, 2015.

[12] L. OpenCFD, "OpenFOAM® - official home of the open source computational fluid dynamics (cfd) toolbox." http://www.openfoam.com/, 2004. [Online; accessed 11-July-2017].

[13] F. R. Menter, "Two-equation eddy-viscosity turbulence models for engineering applications," *AIAA journal*, vol. 32, no. 8, pp. 1598–1605, 1994.

[14] P. R. Spalart and C. L. Rumsey, "Effective inflow conditions for turbulence models in aerodynamic calculations," *AIAA journal*, vol. 45, no. 10, p. 2544, 2007.

[15] B. Kruljevic, "Extension of a local correlation-based transition model in openfoam," diplomityö, 2016-05-16.

[16] F. M. White and I. Corfield, *Viscous fluid flow*, vol. 3. McGraw-Hill New York, 2006. ISBN: 007-124493-X.

[17] W. Frei, "Which turbulence model should i choose for my cfd application?." https://www.comsol.com/blogs/which-turbulence-model-should-choose-cfd-application/, 2013. Accessed: 2017-04-15.

[18] D. Spalding, "A single formula for the law of the wall," *Journal of Applied Mechanics*, vol. 28, no. 3, pp. 455–458, 1961.

[19] D. Coles, "The law of the wake in the turbulent boundary layer," *Journal of Fluid Mechanics*, vol. 1, no. 2, pp. 191–226, 1956.

[20] H. Schlichting, *Boundary-layer theory*. McGraw-Hill, 1968. ISBN: 0-07-055329-7.

[21] M. Morkovin, E. Reshotko, and T. Herbert, "Transition in open flow systems-a reassessment," *Bull. Am. Phys. Soc*, vol. 39, no. 9, p. 1882, 1994.

[22] M. V. Morkovin, "On the many faces of transition," in *Viscous drag reduction*, pp. 1–31, Springer, 1969.

[23] W. S. Saric, H. L. Reed, and E. J. Kerschen, "Boundary-layer receptivity to freestream disturbances," *Annual review of fluid mechanics*, vol. 34, no. 1, pp. 291–319, 2002.

[24] R. Narasimha and K. Sreenivasan, "Relaminarization of fluid flows," *Advances in applied mechanics*, vol. 19, pp. 221–309, 1979.

[25] G. B. Schubauer and H. K. Skramstad, "Laminar-boundary-layer oscillations and transition on a flat plate," tech. rep., National Aeronautics and Space Administration Washington DC, 1948.

[26] J. Dunham, "Predictions of boundary layer transition on turbomachinery blades(predictions of boundary layer transition on turbomachine blades)," *1972.*, pp. 55–71, 1972.

[27] C. Blumer and E. van Driest, "Boundary layer transition-freestream turbulence and pressure gradient effects," *AIAA journal*, vol. 1, no. 6, pp. 1303–1306, 1963.

[28] B. Abu-Ghannam and R. Shaw, "Natural transition of boundary layers - the effects of turbulence, pressure gradient, and flow history," *Journal of Mechanical Engineering Science*, vol. 22, no. 5, pp. 213–228, 1980.

[29] J. Gibbings, *On boundary-layer transition wires*. HM Stationery Office, 1959.

[30] H. Bippes, "Basic experiments on transition in three-dimensional boundary layers dominated by crossflow instability," *Progress in aerospace sciences*, vol. 35, no. 4, pp. 363–412, 1999.

[31] W. S. Saric, R. B. Carrillo, and M. S. Reibert, "Nonlinear stability and transition in 3-d boundary layers," *Meccanica*, vol. 33, no. 5, pp. 469–487, 1998.

[32] D. Arnal and G. Casalis, "Laminar-turbulent transition prediction in three-dimensional flows," *Progress in Aerospace Sciences*, vol. 36, no. 2, pp. 173–191, 2000.

[33] C. Hirsch, *Numerical computation of internal and external flows: The fundamentals of computational fluid dynamics*. Butterworth-Heinemann, 2007. ISBN: 978-0-7506-6594-0.

[34] J. Blazek, *Computational Fluid Dynamics: Principles and Applications*. Elsevier, 2005. ISBN: 0-080-44506-3.

[35] D. Wilcox, *Turbulence Modelling for CFD*. DCW industries Inc., 1993. ISBN: 0-9636051-0-0.

[36] T. Cebeci, *Analysis of Turbulent Flows (2nd Revised and Expanded Edition)*. Elsevier, 2004. ISBN: 978-0-08-044350-8.

[37] F. Menter, M. Kuntz, and R. Langtry, "Ten years of industrial experience with the sst turbulence model," *Turbulence, heat and mass transfer*, vol. 4, no. 1, pp. 625–632, 2003.

[38] B. Launder and B. Sharma, "Application of the energy-dissipation model of turbulence to the calculation of flow near a spinning disc," *Letters in heat and mass transfer*, vol. 1, no. 2, pp. 131–137, 1974.

[39] D. C. Wilcox, "Reassessment of the scale-determining equation for advanced turbulence models," *AIAA journal*, vol. 26, no. 11, pp. 1299–1310, 1988.

[40] F. Menter and T. Esch, "Elements of industrial heat transfer predictions," in *16th Brazilian Congress of Mechanical Engineering (COBEM)*, vol. 109, 2001.

[41] NASA, "Turbulence modeling resource." https://turbmodels.larc.nasa.gov/, 2017. [Online; accessed 24-July-2017].

[42] C. J. Greenshields, *OpenFOAM® Programmer's Guide*. OpeFOAM Foundation Ltd, 2015.

[43] T. Siikonen, "Laskennallisen virtausmekaniikan ja lämmönsiirron perusteet," 2013. (in Finnish).

[44] R. B. Langtry, *A correlation-based transition model using local variables for unstructured parallelized CFD codes*. PhD thesis, University of Stuttgart, 2006.

[45] B. Van Leer, "Towards the ultimate conservative difference scheme i. the quest of monotonicity," in *Proceedings of the Third International Conference on Numerical Methods in Fluid Mechanics*, pp. 163–168, Springer, 1973.

[46] J. P. Boris and D. L. Book, "Flux-corrected transport. i. shasta, a fluid transport algorithm that works," *Journal of computational physics*, vol. 11, no. 1, pp. 38–69, 1973.

[47] H. Jasak, H. Weller, and A. Gosman, "High resolution nvd differencing scheme for arbitrarily unstructured meshes," *International journal for numerical methods in fluids*, vol. 31, no. 2, pp. 431–449, 1999.

[48] P. K. Sweby, "High resolution schemes using flux limiters for hyperbolic conservation laws," *SIAM journal on numerical analysis*, vol. 21, no. 5, pp. 995–1011, 1984.

[49] B. Van Leer, "Towards the ultimate conservative difference scheme. ii monotonicity and conservation combined in a second-order scheme," *Journal of computational physics*, vol. 14, no. 4, pp. 361–370, 1974.

[50] P. L. Roe, "Some contributions to the modelling of discontinuous flows," in *Large-scale computations in fluid mechanics*, pp. 163–193, 1985.

[51] C. J. Greenshields, *OpenFOAM® User Guide version 4.0*. OpenFOAM Foundation Ltd., 2016.

[52] S. V. Patankar and D. B. Spalding, "A calculation procedure for heat, mass and momentum transfer in three-dimensional parabolic flows," *International journal of heat and mass transfer*, vol. 15, no. 10, pp. 1787–1806, 1972.

[53] R. I. Issa, "Solution of the implicitly discretised fluid flow equations by operator-splitting," *Journal of computational physics*, vol. 62, no. 1, pp. 40–65, 1986.

[54] H. K. Versteeg and W. Malalasekera, *An introduction to computational fluid dynamics: the finite volume method*. Pearson Education, 2007. ISBN: 978-0-13-127498-3.

[55] J. Van Ingen, "A suggested semi-empirical method for the calculation of the boundary layer transition region," *Technische Hogeschool Delft, Vliegtuigbouwkunde, Rapport VTH-74*, 1956.

[56] A. M. O. Smith and N. Gamberoni, *Transition, pressure gradient and stability theory*. Douglas Aircraft Company, El Segundo Division, 1956.

[57] R. Mayle and A. Schulz, "Path to predicting bypass transition," *Journal of Turbomachinery. Transactions of the ASME*, vol. 119, no. 3, pp. 405–411, 1997.

[58] F. Menter, T. Esch, and S. Kubacki, "Transition modelling based on local variables. 5th int," in *Symposium on Engineering Turbulence Modeling and Measurements, Mallorca, Spain*, 2002.

[59] OpenFOAM, "C++ source guide." https://cpp.openfoam.org/v4/, 2016. [Online; accessed 15-June-2017].

[60] Zarmehri, "$\gamma - \mathrm{Re}_\theta$ transitional turbulence model tutorial." http://www.tfd.chalmers.se/~hani/kurser/OS_CFD_2012/AyyoobZarmehri/Tutorial_SSTtransition.pdf, 2012. [Online; accessed 23-July-2017].

[61] H. Nilsson, "Implement turbulence model." https://pingpong.chalmers.se/public/courseId/7056/lang-en/publicPage.do?item=3256524, 2016. [Online; accessed 13-March-2017].

[62] A. Savill, "Some recent progress in the turbulence modelling of by-pass transition," *Near-wall turbulent flows*, pp. 829–848, 1993.

[63] G. B. Schubauer and P. Klebanoff, "Contributions on the mechanics of boundary-layer transition," 1956.

[64] J. Nikulainen, "Implementation of a local correlation-based transition model for finflo flow solver," Master's thesis, Imperial College London, 2012.

[65] Coupland, "Ercoftac rolls-royce experimental data." http://cfd.mace.manchester.ac.uk/ercoftac/database/cases/case20/Case_data/, 1990. [Online; accessed 25-June-2017].

Appendices

Appendix A

Discretization and Convergence Studies

A suitable discretization for the convection terms was studied by employing different bounded schemes for the velocity as well as for the turbulence variables (k, ω and γ). An OpenFOAM specific scheme *limitedLinear 1* (see Section 3.3) was used as the applied TVD scheme.

- **Setup 1**: 1st order upwind.
- **Setup 2**: Velocity with the 1st order upwind, turbulence variables with the TVD scheme.
- **Setup 3**: TVD scheme.
- **Setup 4**: TVD (velocity with V-limiter).
- **Setup 5**: 2nd order upwind (velocity with V-limiter).
- **Setup 6**: 2nd order upwind with V-limiter for velocity, turbulence variables with TVD.

All the simulations were performed on T3A test case using the same mesh.

Results

Figure A1 shows the results for the T3A case simulated applying varied setups for the convection schemes. In general, all schemes accomplish to converge with high-order schemes attaining more accurate solutions. The variation between results is minor due to the relatively fine mesh applied on a simple flow case. However, the high-resolution TVD scheme with the V-limiter (Setup 4) surprisingly fails and results in the most inaccurate prediction by delaying the transition roughly 35%. This is most unexpected as the similar setup without the V-limiter achieves a correct prediction for the transition onset. However, no clear reason for this behaviour was observed. Based on the results, the two most accurate setups (3 and 6) were taken into closer examination.

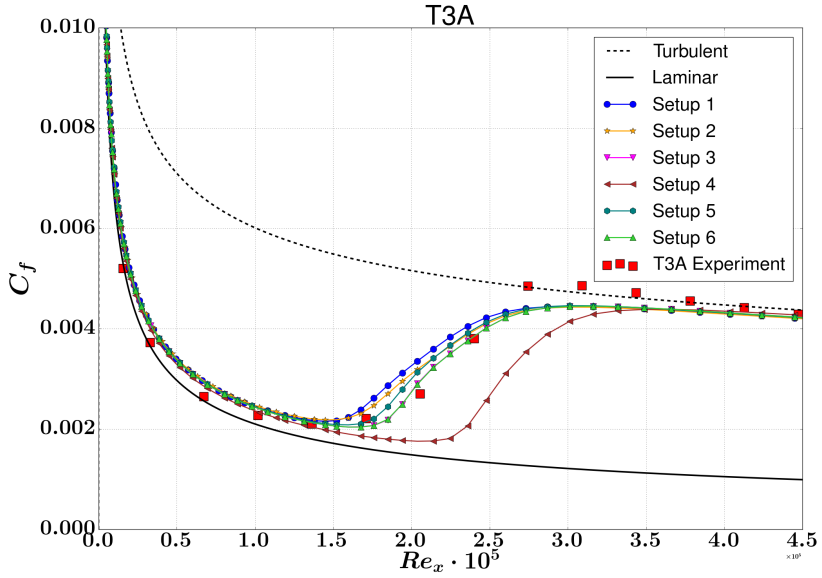

Figure A1: T3A case with different discretizations.

Figures A2a and A2b present the residual convergence for simulations using setup 3 and setup 6, respectively. Although the converge is faster with Setup 3, the solution continues oscillating and the residuals remain clearly on higher levels, especially the pressure residual that achieves only approximately 10^{-2} accuracy. Therefore, the option 6 is selected as the default discretization setup, for which a detailed description can be found from table A1.

Table A1: Default convection schemes for simulations.

Term	Scheme
div(phi,U)	bounded Gauss linearUpwindV grad(U)
div(phi,k)	bounded Gauss limitedLinear 1
div(phi,omega)	bounded Gauss limitedLinear 1
div(phi,im)	bounded Gauss limitedLinear 1

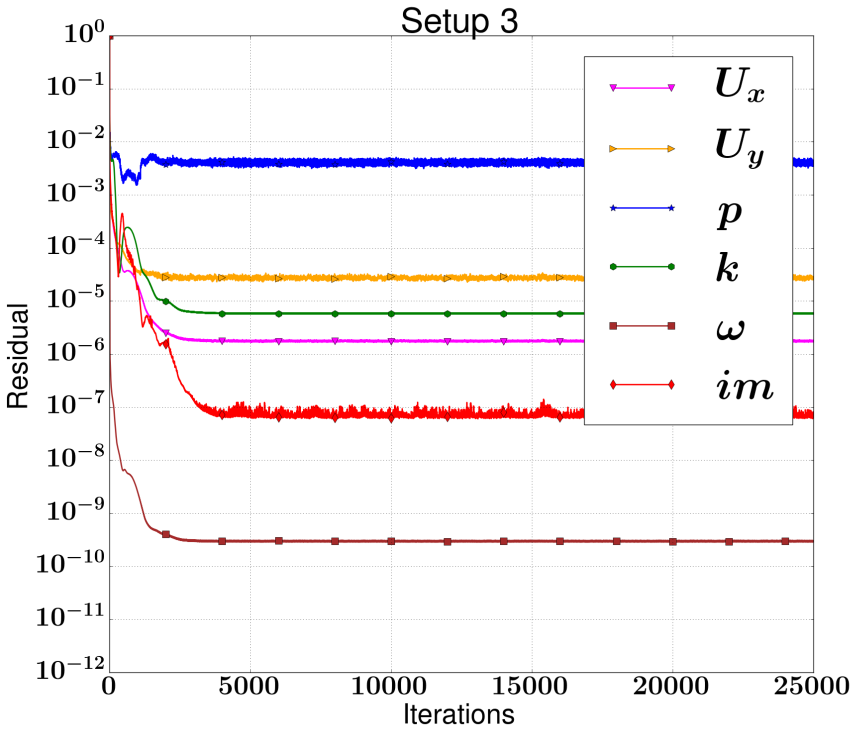

(a)

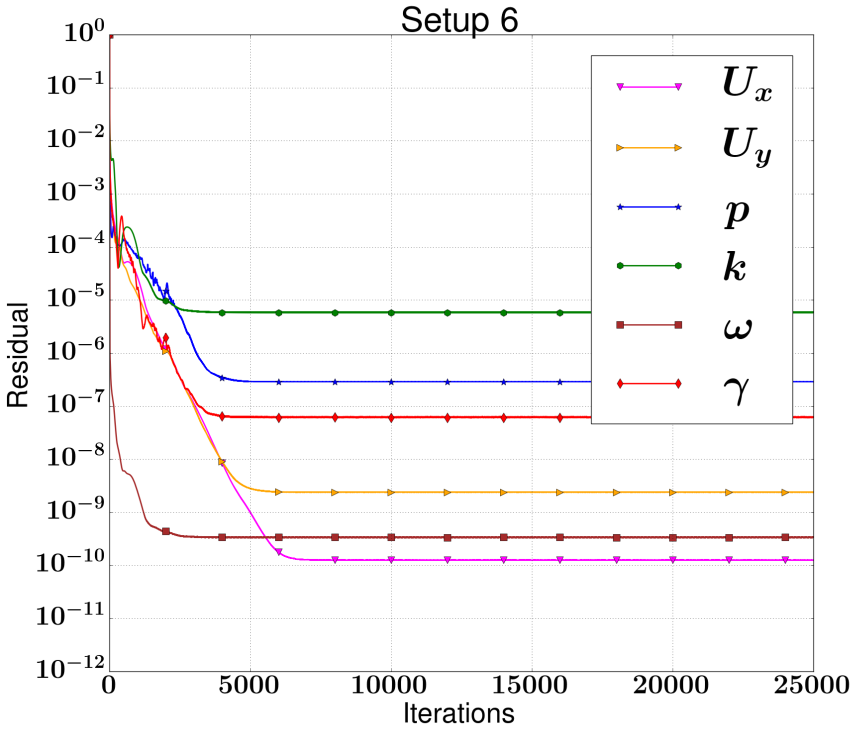

(b)

Figure A2: Convergence

Appendix B

Mesh Convergence Studies

This Appendix shows the results of simulations with the γ-model on verification grids provided by NASA turbulence modelling resource [41]. This was performed in order to investigate the feasibility of standard verification grids for transition modelling. Generating a computational mesh for transition simulations requires additional caution since the transition model needs to solve the thin laminar boundary layer in order to predict the transition. Therefore, a sufficient number of cells are required in normal-to-wall direction within the boundary layer. In addition, the studies by Langtry [44] and Menter [1] have shown that both LCTM models are also sensitive to several other parameters such as, a dimensionless wall distance y^+, a cell expansion rate in both streamwise and normal-to-wall direction, and a number of cells in the streamwise direction. To achieve grid independent solutions, Menter suggests following practice guidelines in mesh construction for the γ-model:

- At least 30 nodes across the boundary layer
- More than 100 nodes in streamwise direction
- The dimensionless wall distance should be less than one: $y^+ < 1$
- The wall normal expansion ratio should be small enough: $R < 1.1$

These are rather strict requirements that are not often met by grids constructed for generic validation cases. In order to examine a feasibility for these type of grids, the model was tested on five different meshes that had varying resolutions from very coarse to highly refined. These grids were designed for two-dimensional zero pressure gradient flat plate cases and created by NASA turbulence modeling resource [41] as a goal to provide resources for CFD developers to verify that models are implemented correctly.

Numerical setup

All the simulations were run on Schubauer-Klebanoff test case, for which the inlet conditions are presented in table 5.3. It should be noted that the length of the inlet

region (0.33 m) in conjunction with a low eddy viscosity ratio ($\mu_t/\mu = 1$) prevented for taking the freestream turbulence decay into account. However, due to a very low level of freestream turbulence intensity ($Tu = 0.03\%$), this had no visible influence on the solution. The applied configuration in the simulations was identical to the ones used in the validation cases (see Section 5.1).

NASA grids have comparatively short normal-to-wall distance of the first cell, as described in table A1, and are refined near the wall and the leading edge, where the highest gradients occur.

Table A1: NASA grids for zero pressure gradient flat plate [41].

Grid	Cells on flat plate	y^+ (S&K)
$2 \times 35 \times 25$	29	0.5
$2 \times 69 \times 49$	57	0.2
$2 \times 137 \times 97$	113	0.1
$2 \times 273 \times 193$	225	0.05
$2 \times 545 \times 385$	449	0.03

NASA grids were converted into OpenFOAM format from the structured 3D-versions of PLOT3D-files.

Results

Figure A1 shows the results for Schubauer-Klebanoff test case simulated on five NASA grids that had different resolutions varying from coarse to highly refined. In general, all grids achieve good prediction for the transition point, except the coarsest mesh ($2 \times 35 \times 25$), which clearly has an insufficient number of cells on the flat plate for solving the correct transition onset. However, an interesting trend on the solutions can be seen as the mesh is refined. An increased resolution shifts the transition point downstream and steepens the curve of the skin friction coefficient. Moreover, the turbulent skin friction remains on slightly higher levels in comparison to the one simulated for the same test case using a mesh constructed according to Menters criteria 5.6d. The reason for this mesh dependency remains unclear as the NASA database does not provide information for all mesh parameters, such as the cell expansion ratio to wall-normal and streamwise direction. The three finest mesh should contain a sufficient amount of cells on the flat plate as well as low enough dimensionless normal-to-wall distance y^+ to model a transition accurately. This dependency related to NASA meshes can be considered to be rather minor source of errors for transition prediction, bearing in mind the other uncertainties in transition modelling. However,

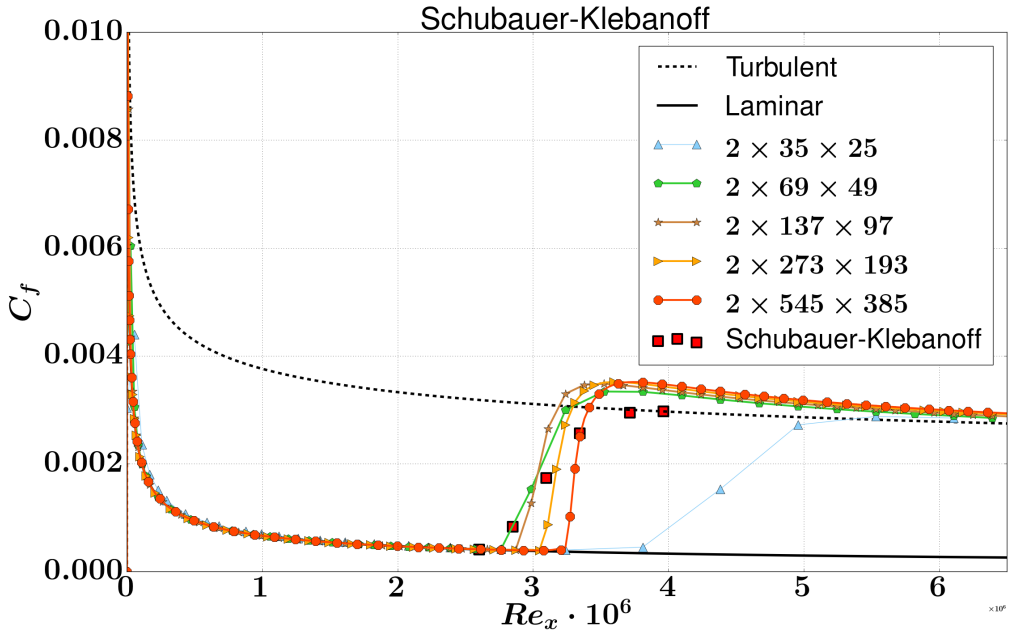

Figure A1: The effect of the grid resolution for the flat plate Schubauer-Klebanoff test case.

Appendix C

Decay of Freestream Turbulence

Several studies have observed unnatural decay of freestream turbulence levels when using SST $k-\omega$ turbulence model [14, 44]. Consequently, due to the inlet region of mesh, the actual turbulence level at the leading edge is significantly lower than at the inlet. This has a significant impact in transition modelling as the process is highly dependent on the freestream turbulence levels.

The decay of the freestream turbulence is dependent on the inlet viscosity ratio (μ_t/μ) with higher ratios reducing the decay. However, too large ratios might influence the underlaying turbulence model by skewing the predicted skin friction results. Therefore, it is suggested by Langtry [44] to use relatively low ratios $(1 \leq \mu_t/\mu \leq 10)$ for transition modelling as the effects of this ratio are still unclear regarding the LCTM models.

The decay of turbulence can be presented in terms of the inlet turbulence intensity (Tu_{in}) and the eddy viscosity ratio (μ_t/μ) by taking into account turbulence model constants (β and β^*) and the inlet region distance x [44]:

$$Tu = \left(Tu_{in}^2 \left[1 + \frac{3\rho U_\infty x \beta Tu_{in}^2}{2\mu(\mu_t/\mu)} \right]^{\frac{\beta^*}{\beta}} \right) \tag{C1}$$

where ρ denotes the density. The turbulence decay described by equation C1 is illustrated in Figure A1, which shows the calculated freestream turbulence intensity with respect to the distance for different eddy viscosity ratios in T3A test case $(Tu = 3.3\%)$. A rapid decay on low eddy viscosity ratios can clearly be observed. It should be emphasized that this limits the length of inlet region of mesh to short distances. For instance, a freestream turbulence intensity of 1.5% at a flat plate leading edge can be obtained with a following combination: $\mu_t/\mu = 10$ and inlet region of length 1.0 [m]. However, when a viscosity ratio of one $(\mu_t/\mu = 10)$ is used, the freestream turbulence intensity decays to value of 1.5% at a distance of 0.1 meter.

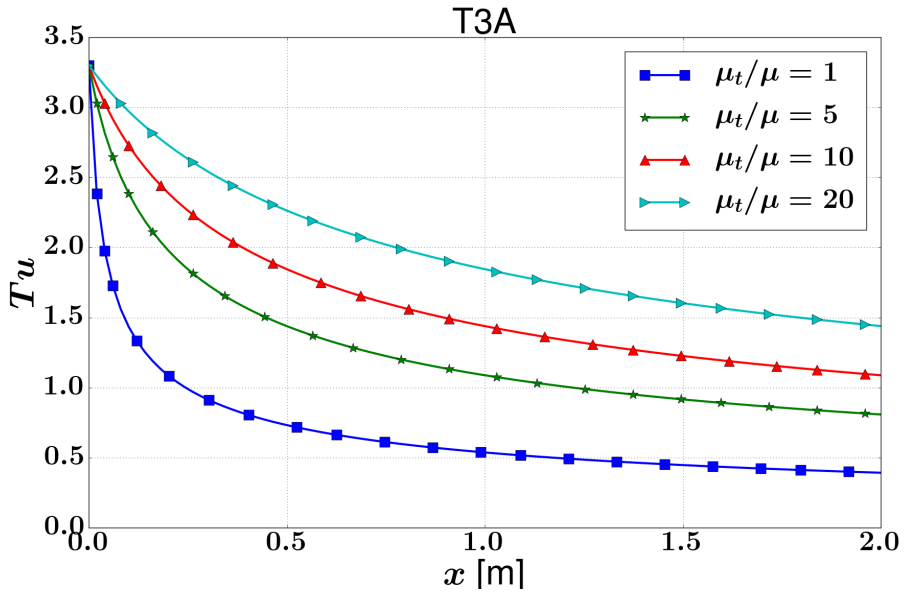

Figure A1: The effect of eddy viscosity ratio on decay of freestream turbulence intensity.